Appendix B

SUPPLEMENTAL INFORMATION FOR CHAPTER 3: GRID FRAP PATTERNING REVEALS A DISPERSIVE EFFECT IN THE BULK OF A LINEARLY CONTRACTING MICROTUBULE NETWORK

B.1 Materials and methods

B.1.1 Motor purification

Plasmids containing the gene encoding the motor-fluorescent protein-light-activated dimerization-FLAG tag construct with the pBiex-1 vector are transfected in Sf9 suspension cells for 60-72 hours at 27°C on shakers rotating at 120 rpm. Cells are then lightly centrifuged at 500 rpm for 12 minutes to remove the supernatant before resuspending in lysis buffer (100 mM NaCl, 2 mM $MgCl_2$, 0.25 mM EDTA, 0.5 mM EGTA, 0.25 % Igepal, 3.5% sucrose by weight, 10 mM imidazole pH 7.5, 10 µg/mL aprotinin, 10 µg/mL leupeptin, 1 mM ATP, 2.5 mM DTT, and 0.5 mM PMSF) and leaving on ice for 20 minutes. Cells are then spun down for 30 minutes at 154k $\times g$ after which the lysate is transferred to tubes containing mouse monoclonal anti-FLAG resin (Sigma A2220) and slowly rotated at 4°C for 1.5$\backsim$3 hrs to allow protein binding to the resin via the FLAG tag. Resin-bound protein are washed three times by spinning down at 2000$\times$ g, clearing the supernatant, then resuspending by tube inversion in wash buffer containing 15 mM KCl, 0.5 mM, 0.1 mM EGTA, 0.1 mM EDTA, 2 mM imidazole pH 7.5, 10 µg/mL aprotinin, 10 µg/mL leupeptin, 0.3 mM DTT, and ATP in 3 mM, 0.3 mM, and 0.03 mM concentrations for the first, second, and third washes, respectively. After the third wash, the protein are spun down again at 2000$\times$ g and most of the supernatant is removed, leaving the resin bed and roughly an equivalent amount of supernatant by volume in the tube. The resin bed is resuspended and FLAG peptide (Sigma F4799 or Thermo Scientific A36805) is added at a final concentration of 0.5 mg/mL before rotating for 3 hrs at 4°C. After incubation to allow the peptide to outcompete the protein for resin binding, the protein are spun down again at 2000$\times$ g with the supernatant extracted and further spun down using centrifuge columns with $\backsim$30 µm pore sizes to further separate proteins from any collected resin beads. Flow-through of clarified protein are spin concentrated

using a 50 kDa filter tube to a final concentration of 2-2.5 mg/mL before diluting in 100% glycerol of the same volume for storage.

B.1.2 Stabilized microtubule polymerization

Fluorescently labeled stabilized microtubules are prepared as in [1, 2]. After flash thawing at 37°C and kept on ice, a combination of ≈ 1.5 mg unlabeled and 100 µg labeled tubulin are diluted to 7.5 mg/mL and 0.5 mg/mL, respectively, in M2B 6.8 containing DTT and GMP-CPP at final concentrations of 1 mM and 6mM, respectively. The tubulin mixture is then incubated on ice for 5 minutes in an ultracentrifuge tube before ultracentrifugation at 90,000 rpm at 4°C for 8 minutes. Avoiding the pellet at the the bottom, the supernatant containing tubulin monomers are then placed in a new Eppendorf tube and incubated at 37°C for 1 hour, typically in a water bath, during which the tubulin is polymerizing and stabilizing with GMPCPP. The microtubule mixture is then aliquoted into individual PCR tubes while constantly being suspended in the mixture by stirring with a pipette tip. PCR tubes are then briefly spun down with a tabletop minicentrifuge before flash-freezing with liquid nitrogen and placed in a -80°C freezer for long-term storage. Microtubules are then prepared for experiments by immersing the PCR tube in 37°C water immediately when taken out of the freezer to quickly thaw.

B.1.3 Glass slide treatment

Corning glass slides and No. 1.5 Deckgläser coverslips are coated with an acrylamide solution to prevent the adhesion of proteins from the light-dimerized activation assay to the surface. The acrylamide coating is done similarly to that demonstrated in [3]. Prior to application of the solution, slides and coverslips are separated by placement in appropriately sized containers and rigorously cleaned through a series of solutions and sonicating. First, slides are immersed in 1% Hellmanex to remove dirt particulates, sonicated, repeatedly rinsed with deionized water (DI H_2O), then repeatedly rinsed with ethanol. Slides are then sonicated in 200 proof ethanol before rinsing again with DI H_2O. After rinsing, slides are sonicated in 0.1 M KOH and subsequently rinsed in double-distilled water (ddH_2O). Finally, trace metals are removed by immersing in 5% HCl for 4 hours. After repeatedly rinsing in ddH_2O, slides are stored overnight with MilliQ ultrapure water.

Upon cleaning and before the acrylamide coating, a silane solution is made first by mixing 98.5% 200 proof ethanol and 1% acetic acid before adding 0.5% trimethoxysilyl methacrylate and immediately pouring into the containers holding the slides and coverslips. After roughly 30 minutes, slides are rinsed twice in 200 proof ethanol before drying with N_2 air and baking at 110°C for 10-15 minutes to cure silane onto surface with oxygen bonding.

The polyacrylamide solution is made by mixing 950 mL ddH_2O with 50 mL 40% acrylamide and degassing under vacuum for 30 minutes. The solution is then under constant mixing on a stir plate with a stir bar during which time 350 µL TEMED and 700 mg ammonium persulfate (APS) are added to the solution. The acrylamide solution is immediately added to the slides and coverslips and incubated overnight. Slides are placed in 4°C for long-term storage.

B.1.4 Flow cell chamber preparation

Flow cells for all light-dimerized activation assays are prepared by thoroughly rinsing an acrylamide-coated glass slide and coverslip in ddH_2O and air drying with N_2 gas. A piece of parafilm with three channels each cut 3 mm wide is placed on the glass slide with the long axis of the channels running along the length of the slide. The coverslip is placed on top of the parafilm with pressure applied to flatten out the film. The flow cell is then briefly placed on a hot plate set at 65°C to warm the parafilm, allowing extra pressure on the contact points between the film and the glass to better seal the chambers.

B.1.5 Light-dimerized activation assay preparation

Photobleaching experiments require an energy mix to maintain stability and function of microtubules and motors while constantly supplying kinesin motors with ATP to contract the microtubule network. This energy mix is slightly altered from that used by Ross *et al.* [1] with the major changes being a change in acidity for K-PIPES from pH 6.8 to pH 6.1 and the absence of catalase to allow for photobleaching. iLid- and micro-tagged motors with the same fluorescent protein are each added to the reaction mixture at final concentrations of 40-100 nM with stabilized microtubules added at a final concentration of 1.5-2.5 µM tubulin. Concentrations of motors and tubulin are tuned to ensure that microtubule network contracts into an aster without an influx of microtubules from outside of the light-activation region.

B.1.6 Optical set-up

The sample is imaged and photobleached using a super planar fluorescence 20x objective from Nikon (numerical aperture 0.45). Image acquisition is performed using a FLiR Blackfly monochrome camera (BFLY-U3-23S6M-C) with two filters in front of it: a Semrock Brightline dual-band pass filter centered at 577 nm (28.3 nm FWHM bandwidth) and 690 nm (55.1 nm FWHM bandwidth) and a Semrock StopLine single-notch filter at 532 nm (17 nm notch bandwidth) to suppress transmission of the YFP YFP excitation to the camera.

Fig. B.1 gives a general idea of the layout of the microscopy components. Activation of motor dimerization and imaging of the microtubules is per-

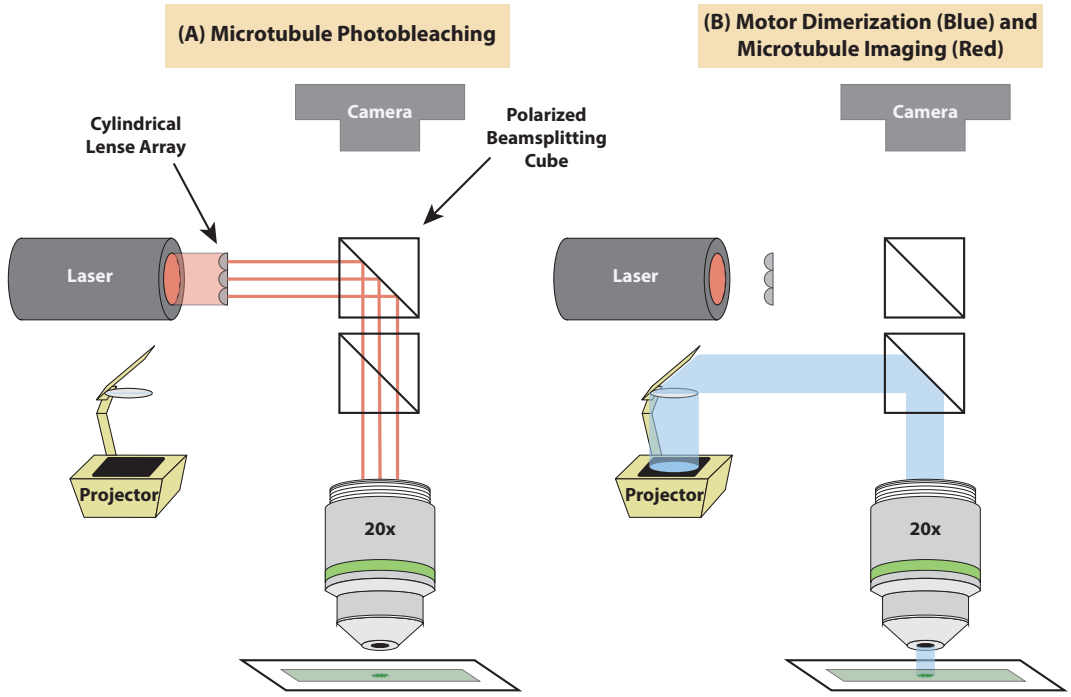

Figure B.1: **Arrangement of the laser and projector.** The laser and projector are set on different optical paths before reaching the sample. (A) The projector shines white light that passes through a filter in order to clip to the desired wavelength. These filters will either transmit blue light to perform the iLid-micro motor dimerization or red light to image the microtubule fluorescence channel. (B) The laser performs the photobleaching of the microtubules in a grid pattern by passing through a cylindrical lens array. The cylindrical lens array is mounted on a rotation mount (not shown) to bleach vertical and horizontal lines. A 20x Nikon objective is used for the imaging.

formed using a digital light projector DLP Lightcrafter Display 4710 EVM Gen2 from Texas Instruments. The DLP projects white light while a motorized filter wheel sets the transmissible range of wavelengths onto the sample (beam blocker for no light, 460/50 nm filter for blue light for iLid-micro dimerization and 630/38 for microtubule imaging). Photobleaching of microtubules is performed using a 645 nm laser. The laser path is set to pass through a cylindrical lens array that transforms the collimated light pattern into a series of lines along one axis. The cylindrical lens array is mounted onto a rotation mount to allow for photobleaching of vertical and horizontal lines to generate the grid pattern. To ensure that the photobleached lines persist for multiple frames of the image, the laser passes through a gimbal-mounted mirror that deflects the beam over a small range of angles. By deflecting the laser light off of the mirror through two lenses with the same focal length f and a second, stationary mirror placed $4 \times f$ away from the gimbal-mounted mirror before passing the laser through the cylindrical lense array, the transformed laser lines can be swept out. We use this beam steering approach to photobleach thicker lines.

To perform the activation and imaging patterns, we supply µManager with a TIFF stacks of matching pixel dimensions as the projector and use a Beanshell script modified from Ross *et al.* to use the correct TIFF image in the stack. The TIFF stack contains a blank image (all pixel values 0) for when the laser is turned on (which is also used in conjunction with the beam blocker to prevent light from passing onto the sample outside of the activation and imaging cycles); a maximum pixel intensity image for the microtubule imaging, and a circular pattern in a blank background for the circular iLid-micro dimerization activation pattern. The primary modification to the Beanshell script is the incorporation of a timer for when the photobleaching will be performed. Once the experiment reaches the desired time, the imaging pauses while the Beanshell script turns on the laser and executes a series of custom written executables that sweep out the laser lines to create thicker parallel photobleached lines, turn off the laser, rotate the cylindrical lense array, then reactivate the laser and sweep out the laser lines in the orthogonal direction to generate the grid pattern. Upon finishing this command, the laser is shut off and imaging resumes. The entire photobleaching is performed within a roughly 10-15 second window.

B.2 Unit cell segmentation and fluorescence preservation in subsequent frames

Fluorescent unit cells of a photobleached microtubule network are segmented in the cropped image sets where the microtubules outside of the activation region are neglected. We first reduce the background signal in each image by performing a heavy Gaussian blur ($\sigma = 20$ pixels) and subtracting off the Gaussian blur from the original image. Images are then normalized to fall between 0 and 1. In order to identify each fluorescent square, we use the triangle thresholding algorithm [4] as it accurately segmented the unit cells in the first image taken after the photobleaching was performed. Other thresholding methods either segmented unit cells to be much smaller and therefore misses a large amount of fluorescent regions of the unit cell or segmented unit cells to be much larger, which affects the amount of time that unit cells are identified as distinct. After the thresholding is applied, the segmented image is cleaned up by removing segmented objects that are too small (less than a third of the area of a unit cell immediately after photobleaching), objects that are too large (more than 3 times larger than an expected unit cell immediately after photobleaching) or images that are too close to the border, which typically removes microtubules outside of the iLid-micro light-dimerized region. To close off any patches within a fluorescent unit cell due to the thresholding, we perform a morphological closing is performed. With the segmented images, the centroid position, area, and total fluorescence of each unit cell are obtained as well as the pixel-weighted centroid of the entire segmented image to obtain the microtubule network center.

Subsequent images of the same dataset undergo the same background subtraction to segmented image clean-up. However, as the some fraction of the fluorescent microtubules begin to disperse, the image segmentation may not pick up fewer of the fluorescent microtubules at the boundary of the unit cell with the photobleached region as they may be considered too low in signal to be distinguished from the background. As a result, for later images than the first image after photobleaching, we correct the segmentation by adding on pixels around the boundary of the segmented unit cells until we return to the correct total fluorescence. To do this, each unit cell is then paired with itself from the previous time step by determining nearest centroids. Due to the minimal reduction in fluorescence intensity from the DLP during imaging as shown in Section B.3, we compare the total fluorescence intensity of the unit

cell in the frame of interest post-segmentation to its total intensity from the first frame. If the total intensity is less than 99% of the initial intensity, we continually add a single-pixel thick layer around the unit cell until the unit cell finally falls within 99% of the initial intensity. If after an iteration the total intensity becomes greater than the initial intensity, we remove the dimmest pixel around the outer layer until the intensities roughly match. Unit cell centroids, areas, and fluorescence intensities are then computed in addition to the pixel-weighted center of the entire contracting network after this intensity-adjusted processing for all of the unit cells. Image processing of a unit cell terminates when it is found to overlap with another unit cell during the fluorescence intensity correction scheme as this indicates that the unit cells have begun to merge and by the next time point will no longer be distinguished.

B.3 Projector effects on microtubule fluorescence intensity

In analyzing the photobleached microtubule field as the network contracts, we used the total fluorescence intensity of the unit cells as a conserved quantity during the unit cell segmentation. One concern might be whether the microtubule fluorescence decreases in time due to the effects of the projector, which illuminates the field of view for imaging purposes. To investigate this, we imaged the microtubule field without activating the iLid-micro dimerization using the same exposure times ($\backsim$100 ms) and imaging frequency (10 s per frame). We then examined the mean image intensity and standard deviation of the pixel intensity as a function of time.

SI Fig. B.2(A) illustrates the effects of the projector on the microtubule field. The mean intensity of the field of view, as normalized against the mean intensity at $t = 0$ seconds, indicates that the fluorescence field fluctuates only a few tenths of a percent but does not appear to decrease over an hour. These fluctuations are likely due to the diffusion of the microtubules in the flow cell, as SI Fig. B.2(B) shows the normalized mean intensity of the microtubule fluorescence channel but in the absence of microtubules. Here, we see that that there are fewer fluctuations in the fluorescence intensity, further supporting that the small fluctuations in fluorescence intensity in successive imaging stages comes from diffusion of the microtubules. Nevertheless, we show here that the fluorescence intensity is well preserved and use this as our justification for using total fluorescence intensity as the conserved metric for unit cell segmentation.

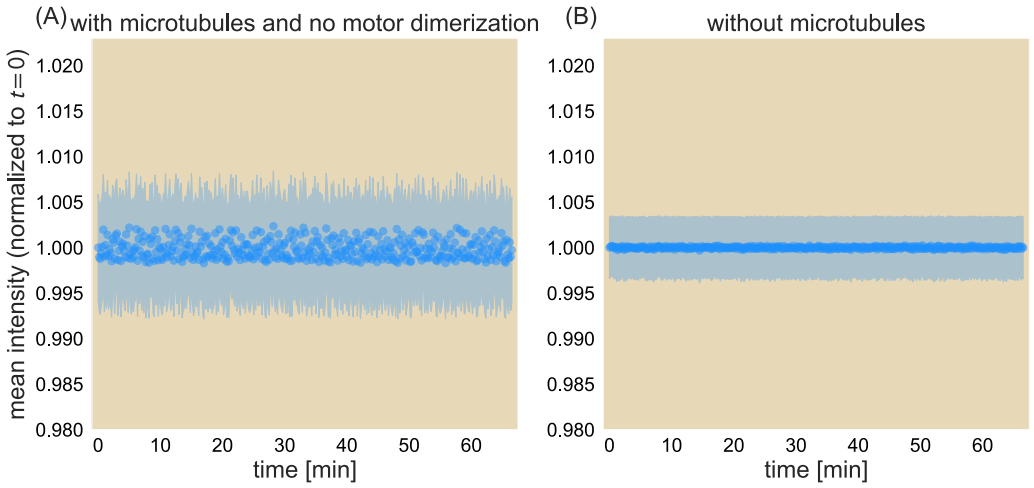

Figure B.2: **Image intensity of the microtubule field as a function of time.** (A) Mean intensity of the microtubule field normalized against that of the first image. Blue shaded region represents one standard deviation in the mean intensity (normalized by the same initial mean value). (B) Mean intensity of the same fluorescence channel in the absence of microtubules. Blue shaded region once again represents the standard deviation of the image region.

B.4 Data analysis

B.4.1 Contraction rate computation

In the main text, we use the centroids of fluorescent unit cells obtained as outlined in Section B.2 of Appendix B to demonstrate that contraction speed of the microtubule network scales linearly with distance from the network center. We first obtain the speed that each unit cell centroid is moving toward the center as a function of time. For each unit cell, we observe a linear relation between the centroid distance from the network center and time after photobleaching of the form

$$r = v_c\, t + r_0, \tag{B.1}$$

where r is the unit cell centroid distance from the network center, v_c is the speed of the unit cell (which will take to be positive here but directed toward the origin), t is the time since photobleaching, and r_0 is the initial centroid distance from the network center immediately after photobleaching.

Using the extracted contraction speed and distances for all of the unit cells for a given motor type, we next computed the rate of contraction of the microtubule network. We note that we expect a linear relation between radius r and centroid speed v_c of the form

$$v_c = \alpha\, r + v_0, \tag{B.2}$$

where α is the contraction rate and v_0 is the contraction speed at the network center. Although we expect the speed at the network center to be 0, we relax this assumption for our analysis. To more carefully compute the rate of contraction of the network and determine the range of credibility of the computed rate, we use a Bayesian approach. Specifically, we compute the probability of α and v_0 given our data on the contraction speeds for each unit cell and their distance from the network center, $P\left[\alpha, v_0 | \left\{(r_0, v_c)_i\right\}\right]$, where i denotes each unit cell. Here, we use the centroid distance immediately after photobleaching but found that another criterion such as the median of the centroid distance over the course of the time window analyzed does not dramatically affect the results due to the relatively small travel $\left(\frac{\Delta r}{r_0} < 10\% \text{ for } \Delta r \text{ the distance traveled over the entire time course}\right)$ the unit cells undergo.

We note from Bayes' Theorem that

$$\begin{aligned} P\left[\alpha, v_0 | \left\{(r_0, v_c)_i\right\}\right] &= \frac{P\left[\left\{(r_0, v_c)_i\right\} | \alpha, v_0\right] P\left(\alpha, v_0\right)}{P\left[\left\{(r_0, v_c)_i\right\}\right]}, \\ &= \frac{\prod_i P\left[(r_0, v_c)_i | \alpha, v_0\right]}{\prod_i P\left[(r_0, v_c)_i\right]} P\left(\alpha, v_0\right), \\ &\propto \prod_i P\left[(r_0, v_c)_i | \alpha, v_0\right] P\left(\alpha, v_0\right), \end{aligned} \tag{B.3}$$

where we drop the denominator on the right-hand side as it does not involve the parameters we want to find, thus making the two sides proportional to each other. Here, $P\left[(r_0, v_c)_i | \alpha, v_0\right]$ is the likelihood distribution of getting the $(r_0, v_c)_i$ that we did given α and v_0 while $P\left(\alpha, v_0\right)$ is the prior distribution of our two parameters.

We expect that our priors on α and v_0 are independent of each other, so we can break up the probability function into a product of two:

$$P\left(\alpha, v_0\right) = P\left(\alpha\right) P\left(v_0\right). \tag{B.4}$$

Meanwhile, we can rearrange each likelihood function as a product of two probabilities. The probability of getting $(r_0, v_c)_i$ given our parameters is also the probability of getting $v_{c,i}$ given our parameters and $r_{0,i}$ times the probability of getting $r_{0,i}$, or

$$\begin{aligned} P\left[(r_0, v_c)_i | \alpha, v_0\right] &= P\left(v_{c,i} | \alpha, v_0, r_{0,i}\right) P\left(r_{0,i}\right), \\ &\propto P\left(v_{c,i} | \alpha, v_0, r_{0,i}\right), \end{aligned} \tag{B.5}$$

where we change to a proportionality again as $P(r_{0,i})$ is independent of our parameters. Here, we expect that our contraction speed for a given unit cell $v_{c,i}$ comes from a Normal distribution where the mean value is $\alpha\, r_{0,i} + v_0$ and standard deviation σ. This means that we will also need a prior on σ. This means that our distribution really takes the form of

$$P\left[\alpha, v_0, \sigma | \left\{(r_0, v_c)_i\right\}\right] \propto P(\alpha)\, P(v_0)\, P(\sigma) \prod_i P\left(v_{c,i} | \alpha, v_0, \sigma, r_{0,i}\right). \tag{B.6}$$

As a result, we say that our likelihood takes the form

$$v_{c,i} \backsim \text{Normal}\left(\alpha r_{0,i} + v_0, \sigma^2\right). \tag{B.7}$$

We then defined our priors to be that α is drawn from the half-normal distribution where $\alpha > 0$ as we are working with speeds of contraction, σ is also drawn from a half-normal distribution and enforced to be positive, and v_0 is drawn from a normal distribution about $v = 0$. We make the offset a normal rather than a half-normal distribution as there may be a value of $r > 0$ for which the contraction stops, which for a positive slope would mean a negative speed at $r = 0$. Put together, we have the following priors:

$$\alpha \backsim \text{Half-Normal}(0, 1), \tag{B.8}$$

$$\sigma \backsim \text{Half-Normal}(0, 1), \tag{B.9}$$

$$v_0 \backsim \text{Normal}(0, 1). \tag{B.10}$$

We sampled the joint distribution of (α, v_0, σ) by Hamiltonian Markov chain Monte Carlo using the Stan probabilistic program [5]. From each (α, v_0) that is sampled we compute the mean value $\mu = \alpha\, r + v_0$ for $0 \leq r \leq R$ where R is the distance of the farthest centroid from the network center and report the median and 95% credible region for at each distance r as presented in Fig. 2 of the main text and Fig. B.6.

B.5 Deformation of a square due solely to contraction

In the main text, we observed that each fluorescent unit cell on average conserves its area while its center of mass moves toward the network center with speed that is linearly dependent on the distance from the center. We compute the expected area of each unit cell had the network elastically contracted due solely to the observed global contraction. We define the contraction velocity field $\mathbf{v}(x, y)$ as

$$\mathbf{v}(x, y) \equiv -\alpha\left(x\hat{x} + y\hat{y}\right), \tag{B.11}$$

where α is the contraction rate as computed in SI Sec. B.4.1 and reported in the main manuscript. This means that after a time interval Δt a point (x, y) subject to this advective flow will be displaced in the x- and y- directions according to

$$\begin{aligned} dX &= -\alpha x \Delta t, \\ dY &= -\alpha y \Delta t, \end{aligned} \tag{B.12}$$

so the point at the later time (x', y') relates to its earlier time point by

$$\begin{aligned} x' &= x + dX = x\left(1 - \alpha \Delta t\right) \\ y' &= y + dY = y\left(1 - \alpha \Delta t\right). \end{aligned} \tag{B.13}$$

Suppose we looked at the four corners of a unit cell, labeled as A, B, C, D as depicted in Fig. B.3. If we assign their coordinates as

$$\begin{aligned} \mathrm{A} &\to \left(x_{\mathrm{A}}, y_{\mathrm{A}}\right), \\ \mathrm{B} &\to \left(x_{\mathrm{B}}, y_{\mathrm{B}}\right), \\ \mathrm{C} &\to \left(x_{\mathrm{C}}, y_{\mathrm{C}}\right), \\ \mathrm{D} &\to \left(x_{\mathrm{D}}, y_{\mathrm{D}}\right), \end{aligned} \tag{B.14}$$

we see that by picking a square, we can simplify any two diagonal points to be dependent on coordinate values from the other two diagonal points, so with a choice of using coordinates from A and D, the coordinates become

$$\begin{aligned} \mathrm{A} &\to \left(x_{\mathrm{A}}, y_{\mathrm{A}}\right), \\ \mathrm{B} &\to \left(x_{\mathrm{D}}, y_{\mathrm{A}}\right), \\ \mathrm{C} &\to \left(x_{\mathrm{A}}, y_{\mathrm{D}}\right), \\ \mathrm{D} &\to \left(x_{\mathrm{D}}, y_{\mathrm{D}}\right). \end{aligned} \tag{B.15}$$

Under the deformation mapping, their new coordinates, labeled as A′, B′, C′, and D′ get mapped on as

$$\begin{aligned} \mathrm{A}' &\to \left[x_{\mathrm{A}}\left(1 - \alpha \Delta t\right), y_{\mathrm{A}}\left(1 - \alpha \Delta t\right)\right], \\ \mathrm{B}' &\to \left[x_{\mathrm{D}}\left(1 - \alpha \Delta t\right), y_{\mathrm{A}}\left(1 - \alpha \Delta t\right)\right], \\ \mathrm{C}' &\to \left[x_{\mathrm{A}}\left(1 - \alpha \Delta t\right), y_{\mathrm{D}}\left(1 - \alpha \Delta t\right)\right], \\ \mathrm{D}' &\to \left[x_{\mathrm{D}}\left(1 - \alpha \Delta t\right), y_{\mathrm{D}}\left(1 - \alpha \Delta t\right)\right]. \end{aligned} \tag{B.16}$$

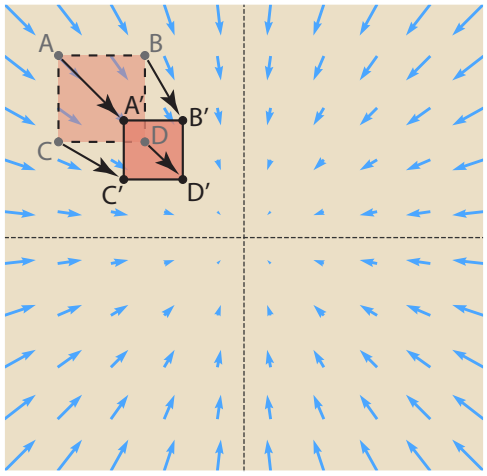

Figure B.3: **Schematic of unit cell contraction due purely to the advective velocity field.** An advective velocity field scales linearly with distance from the origin while pointing radially inward and are shown in blue. The points at the corners of the square (A, B, C, D) are mapped after some time Δt to (A′, B′, C′, D′).

Eqs. B.16 tells us that under this particular velocity field, any two points that are horizontally or vertically aligned will maintain the same horizontal or vertical alignment, respectively, even at later times. Thus, a square will preserve its shape in time.

We next examine what happens to the area of a unit cell had the only effect been the global contraction. In this case, we can compare the area of the square before and after the deformation. To compute the area swept out by (A,B,C,D), we multiply the line segment between B and D, L_{BD} with the line segment between C and D, L_{CD}:

$$\begin{aligned}\sigma_{(\mathrm{A,B,C,D})} &= L_{\mathrm{BD}} \times L_{\mathrm{CD}}, \\ &= \left[\sqrt{(x_{\mathrm{B}} - x_{\mathrm{D}})^2 + (y_{\mathrm{B}} - y_{\mathrm{D}})^2}\right] \times \left[\sqrt{(x_{\mathrm{D}} - x_{\mathrm{C}})^2 + (y_{\mathrm{D}} - y_{\mathrm{C}})^2}\right], \\ &= (y_{\mathrm{A}} - y_{\mathrm{D}}) \times (x_{\mathrm{D}} - x_{\mathrm{A}}), \end{aligned} \tag{B.17}$$

where we use Eq. B.15 to write in terms of the coordinates of A and D. In comparison, the area of the deformed unit cell swept out by (A′, B′, C′, D′)

takes the form

$$\begin{aligned}
\sigma_{(\mathrm{A}',\mathrm{B}',\mathrm{C}',\mathrm{D}')} &= L_{\mathrm{B}'\mathrm{D}} \times L_{\mathrm{C}'\mathrm{D}'}, \\
&= \left[\sqrt{\left(x_{\mathrm{B}'} - x_{\mathrm{D}'}\right)^2 + \left(y_{\mathrm{B}'} - y_{\mathrm{D}'}\right)^2}\right] \times \left[\sqrt{\left(x_{\mathrm{D}'} - x_{\mathrm{C}'}\right)^2 + \left(y_{\mathrm{D}'} - y_{\mathrm{C}'}\right)^2}\right], \\
&= \left(y_{\mathrm{A}'} - y_{\mathrm{D}'}\right) \times \left(x_{\mathrm{D}'} - x_{\mathrm{A}'}\right), \\
&= \left[y_{\mathrm{A}}\left(1 - \alpha\Delta t\right) - y_{\mathrm{D}}\left(1 - \alpha\Delta t\right)\right] \times \left[x_{\mathrm{D}}\left(1 - \alpha\Delta t\right) - x_{\mathrm{A}}\left(1 - \alpha\Delta t\right)\right], \\
&= \left(y_{\mathrm{A}} - y_{\mathrm{D}}\right)\left(1 - \alpha\Delta t\right) \times \left(x_{\mathrm{D}} - x_{\mathrm{A}}\right)\left(1 - \alpha\Delta t\right), \\
&= \left(y_{\mathrm{A}} - y_{\mathrm{D}}\right) \times \left(x_{\mathrm{D}} - x_{\mathrm{A}}\right)\left(1 - \alpha\Delta t\right)^2, \\
&= \sigma_{(\mathrm{A},\mathrm{B},\mathrm{C},\mathrm{D})}\left(1 - \alpha\Delta t\right)^2. \qquad \text{(B.18)}
\end{aligned}$$

Thus we find that the area of the unit cell subject solely to the contraction would decrease by $(1 - \alpha\Delta t)^2$ after a time period Δt. This comes in contrast to the results that we present here where the area of the fluorescent unit squares remains constant during the contraction process suggesting a mechanism that disperses microtubules against the global contraction.

B.6 Microtubule length extraction

Stabilized microtubules imaged under total internal reflection fluorescence (TIRF) microscopy such as the ones shown in Fig. B.4A were analyzed similar to that discussed in [1] in order to extract their lengths. Briefly, due to the even illumination that can occur in the image, images were first background corrected using a local thresholding method known as Niblack thresholding [6] with window size of 3 pixels and k value of 0.001, which determines how many standard deviations below the mean pixel value that one sets the cut-off within the window. Although the array is a series of pixel values to be weighed against the original image, we found that this array already improved the image contrast. Due to better flattening of the image but a nonbinary image, we used Otsu thresholding on the Niblack theshold array to extract the microtubules from the background. The result is shown in Fig. B.4B.

Using the binary image which contains extracted microtubules, we imposed a morphological closing algorithm to reconnect any microtubules that were broken during the Niblack thresholding from being picked up as signal. This closing was performed using a 3 pixel x 3 pixel square array, suggesting that disconnected microtubules needed to be within $3\sqrt{2}$ pixels of each other at their ends to be connected again. From here, we removed any microtubules

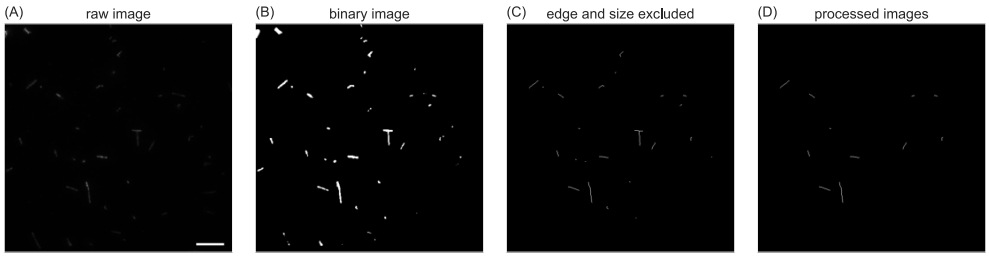

Figure B.4: **Processing steps of microtubule images.** (A) Raw image. Scale bar denotes 10 µm. (B) Images processed after computing a Niblack threshold and using Otsu thresholding on the Niblack threshold array. (C) Putative MTs skeletonized after removing objects too close to the image border or too small. (D) Removal of any MTs that cross over each other to get the final MTs used for analysis.

that were too close to the edge of the image as they may extend outside of the camera field of view, any objects that were fewer than 10 pixels in area as we considered them too small to know with enough certainty whether they were microtubules or small blemishes in the image. Putative microtubules underwent a morphological thinning so that they were converted to one-pixel wide lines along which we could compute their lengths. The result of the edge and size exclusion and skeletonizing are shown in Fig. B.4C.

As a final step before measuring the lengths, we removed any microtubules that seemed to cross over. This was performed by removing objects where two line segments along the same microtubule strand formed angles of at least 75°, leaving behind a processed image such as Fig. B.4D. From here, we used any remaining microtubules and measured their lengths and compiled them. Fig. B.5 shows empirical cumulative distribution functions of these microtubules from the four MT polymerization assays performed over the course of the work presented here. n denotes the number of microtubules that were extracted from the image processing and used in the ECDF for each replicate. Here, we see that for most of the work performed the MTs had lengths between $1 - 3$ µm with median lengths between $1.5 - 2$ µm.

B.7 Motor constructs

While several of the motors used here in the analysis are obtained from previous work, including K401 expressed in bacteria [1], K401 expressed in insects and Ncd236 expressed in insects [7], we also designed constructs for the study of Ncd281 [8]. Specifically, the sequences are inserted into pBiex-1 vectors and

Motor Construct	Sequence Layout
micro variant	pBiex-1:FLAG-GG-mVenus-$(GSG)_2$-micro-$(GSG)_4$-Ncd281
iLid variant	pBiex-1:FLAG-GG-mVenus-$(GSG)_2$-iLid-$(GSG)_4$-Ncd281

Table B.1: **Ncd281 construct design.** All constructs are designed in the pBiex-1 vector and produced by Twist Biosciences.

includes a FLAG tag for protein purification, mVenus for motor fluorescence visualization, either a micro or iLid domain as described in [9] and Ncd281 as described in [8]. Between these different domains are multiple repeats of a 'GSG' amino acid sequence which offers flexible links between the regions. Table B.1 illustrates these sequences. Constructs were produced by Twist Biosciences.

B.8 Measuring motor speeds and their effects on contraction rate and unit cell area

In the work shown in the main manuscript, we showed that by changing the motor used in the system from Ncd236 to the slower Ncd281 the contraction

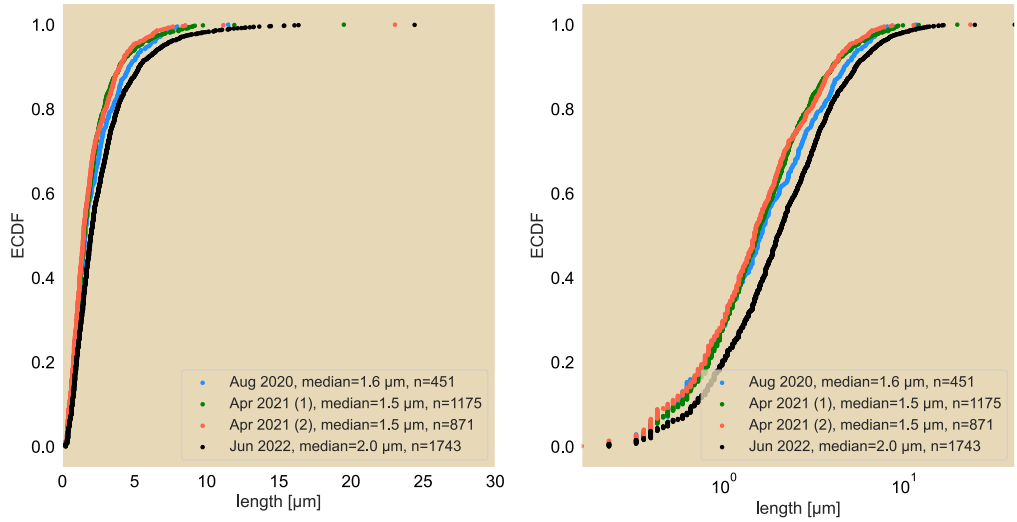

Figure B.5: **Empirical cumulative distributions of microtubule length from microtubules stabilized from polymerization preparations for experiments used in this manuscript.** Microtubules were prepared four times over the course of the work presented here, thus shown as four different datasets. Left and right plots show the same data but on different x-scales (linear for the left plot and logarithmic scale on the right). The two polymerization preparations performed in April 2021 were performed separately by two of the authors of this manuscript on the same day. n denotes the number of microtubules whose lengths were used in the ECDFs.

rate of the microtubule network decreased while the unit cell area remained uniform in time, suggesting that motor speed largely drives a local reorganization of the microtubules in the bulk of the network despite the global contraction. We similarly performed our photobleaching approach to the active contraction assay on two motors that are faster than Ncd236. Both are K401 constructs with one expressed in bacteria as in [1] while the other is expressed in insects from the constructs designed in [7]. These motors have different speeds, which we measure through gliding assays.

Fig. B.6 shows the effects of the different motor speeds on contraction speed as a function of distance from the center of the contracting network and normalized area as a function of time. Unlike Ncd281 (column B) where the contraction rate decreases relative to Ncd236 (column A), the insect-expressed (column C) and bacterial-expressed (column D) K401, both of which are faster than Ncd236, the contraction rate increases. Interestingly, despite the bacterial K401 being slower than the insect K401, they have similar contraction rates, with contraction rates of $0.0065^{+0.0009}_{-0.0008}$ s^{-1} and 0.0072 ± 0.0012 s^{-1}, respectively. Even so, we find that despite dramatic increases the contraction rate, the unit cell areas on average remain constant.

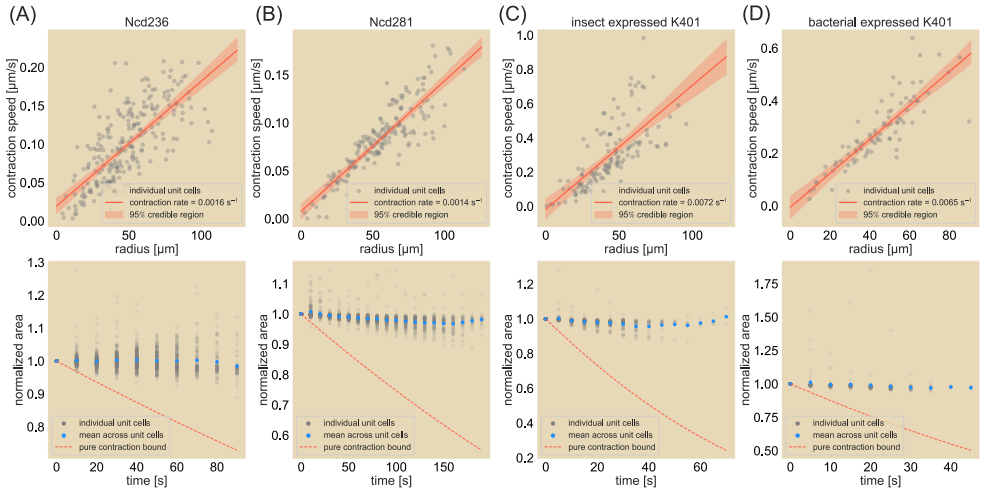

Figure B.6: **Contraction rates and unit cell area in time for four different motors.** (Top row) Contraction speed against radius for unit cell centroids with most likely contraction rate fit (red line) and 95% credible region (shaded region) and (bottom row) unit cell area as a function of time for (A) Ncd236, (B) Ncd281, (C) K401 expressed in insect cells, and (D) K401 expressed in bacteria.

B.9 The recovery of a typical FRAP-like disc is time-sensitive in the advection-diffusion model

As we derive in the Section B.12, the general solution to the PDE

$$\frac{\partial c}{\partial t} = D\nabla^2 c + \nabla \cdot \left[\frac{v_{\mathrm{m}}}{R}\mathbf{r}c\right], \tag{B.19}$$

assuming no angular dependence takes the form

$$c(r,t) = c_{\mathrm{ss}}\, e^{-\frac{r^2}{2\lambda^2}} + e^{-\frac{r^2}{2\lambda^2}} \sum_{i=1}^{\infty} c_i e^{-Dk_i^2 t}\, {}_1F_1\Big(-\frac{\lambda^2 k_i^2}{2}; 1; \frac{r^2}{2\lambda^2}\Big), \tag{B.20}$$

where c_{ss} is the coefficient for the steady-state concentration term, $\lambda \equiv \sqrt{\frac{DR}{v_{\mathrm{m}}}}$, k_i are the eigenvalues specific to the boundary condition, c_i are the coefficients based on initial conditions, and ${}_1F_1(a;b;z)$ is the Kummer confluent hypergeometric function

$${}_1F_1(a;b;z) = \sum_{l=0}^{\infty} \frac{(a)_l}{(b)_l}\frac{z^l}{l!}, \tag{B.21}$$

where the Pochhammer symbol $(a)_l = \frac{(a+l-1)!}{(a-1)!}$. The most well-known example of Eq. B.21 is the case where $a = b$, which yields ${}_1F_1(a;a;z) = e^z$. The eigenvalues $\{k_i\}$ are found by satisfying the boundary conditions and are those terms that satisfy the equation

$$\Big(\frac{\lambda^2 k_i^2}{2}\Big){}_1F_1\Big(1 - \frac{\lambda^2 k_i^2}{2}; 2; \frac{R^2}{2\lambda^2}\Big) = 0. \tag{B.22}$$

Eq. B.80 shows that the steady-state profile of the concentration is a Gaussian distribution with standard deviation λ.

We now seek to identify the coefficients of the terms, which are specific to the initial conditions. Here, we will analytically examine three cases for initial conditions: 1) uniform concentration, 2) a uniform concentration except with molecules removed in the region $r \le R_0$ as found in many FRAP assays, and 3) a FRAP-like removal of molecules in the region $r \le R_0$ after the system initially reaches a steady-state Gaussian concentration profile.

B.9.1 Uniform concentration

We start with the case where the concentration is uniform everywhere:

$$c(r,0) = c_0. \tag{B.23}$$

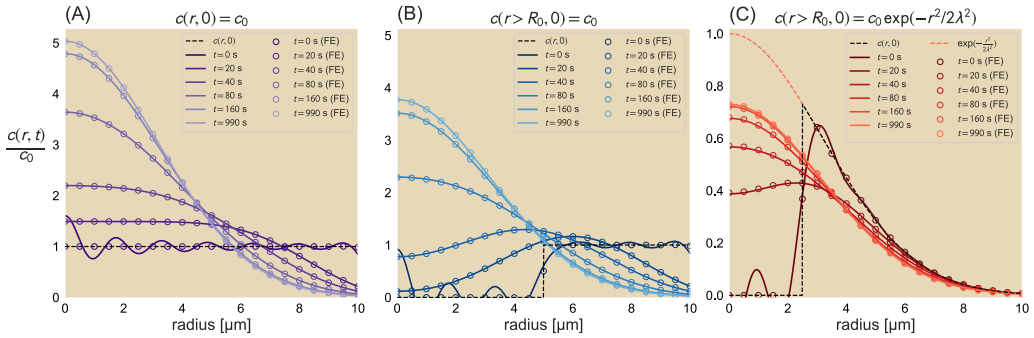

Figure B.7: **Radial advection-diffusion for various initial conditions.** (A) Uniform concentration throughout the system. (B) Uniform concentration for $r > R_0$ and no molecules for $r \leq R_0$. (C) A Gaussian distribution for $r > R_0$ and no molecules for $r \leq R_0$. Analytical solutions are presented as solid lines while solutions obtained by finite elements are shown as hollow points. The initial condition for each situation is shown as a dashed red line. For all studies, $D = 0.1\,\frac{\mu m^2}{s}$, $R = 10$ μm, and $v_m = 0.1\,\frac{\mu m}{s}$. For (B), we set $R_0 = \frac{R}{2}$ while for (C) we set $R_0 = \frac{R}{4}$. For (C), the steady-state profile prior to removing molecules for $r \leq R_0$ is shown as a dashed red line. All analytical solutions use the first 12 eigenvalues that satisfy Eq. B.79.

The solution to the PDE with this initial condition takes the form of

$$c(r,t) = \frac{c_0}{2} e^{-\frac{r^2}{2\lambda^2}} \Bigg\{ \frac{\frac{R^2}{\lambda^2}}{1 - e^{-\frac{R^2}{2\lambda^2}}} + \sum_{i=1}^{\infty} \frac{R^2\, e^{-D\,k_i^2 t}\, {}_1F_1\Big(-\frac{\lambda^2 k_i^2}{2}; 2; \frac{R^2}{2\lambda^2}\Big)}{\int_0^R r'\, e^{-\frac{r'^2}{2\lambda^2}} \Big[{}_1F_1\Big(-\frac{\lambda^2 k_i^2}{2}; 1; \frac{r'^2}{2\lambda^2}\Big)\Big]^2 \mathrm{d}r'} \times {}_1F_1\Big(-\frac{\lambda^2 k_i^2}{2}; 1; \frac{r^2}{2\lambda^2}\Big) \Bigg\}. \tag{B.24}$$

Fig. B.7A shows the concentration profile as a function of radius and for various time points given this initial condition. Here, we used $D = 0.1\,\frac{\mu m^2}{s}$, $R = 10$ μm, and $v_m = 0.1\,\frac{\mu m}{s}$. Solid lines indicate different time points for the specific analytical solution given the uniform initial condition. These analytical solutions also show strong agreement with simulations performed by FEM which are denoted by hollow points. Here, we use the first 12 eigenvalues k_i for the analytical solution. Similar to the decomposition of a square wave into a sum of sinusoidal functions yielding imperfect agreement with the original function, we see here that the use of a limited number of eigenvalues that satisfy Eq. B.79 leads to fluctuations about the original function for $t = 0$ (see Appendix B.14 on Gibbs phenomenon). Nevertheless, we see that these

fluctuations in the analytical condition quickly smooth out for $t > 0$. For the given parameters, the concentration at larger radii decreases quickly due to the higher advection overcoming diffusion. As shown at $t = 20$ seconds and $t = 40$ seconds, the concentration appears roughly uniform at lower concentrations but the length scale of this uniformity appears to decrease. At $t = 990$ seconds, the concentration profile reaches the Gaussian steady-state solution where the concentration gradient allows diffusion to counter the advective flow.

B.9.2 Uniform concentration for $r > R_0$

We apply a similar initial condition as that used in Sec. B.9.1, but remove any molecules within a distance R_0 from the origin as typically performed in FRAP experiments. This initial condition is mathematically described by

$$c(r,0) = \begin{cases} 0 & \text{if } r \leq R_0, \\ c_0 & \text{if } r > R_0. \end{cases} \tag{B.25}$$

The solution for this initial condition is similar to Eq. B.24 but with different limits of integration (see Appendix B.11 on Sturm-Liouville Theory and S2 for application of the theory in 2D):

$$c(r,t) = \frac{c_0}{2} e^{-\frac{r^2}{2\lambda^2}} \left\{ \frac{\frac{R^2}{\lambda^2} - \frac{R_0^2}{\lambda^2}}{1 - e^{-\frac{R^2}{2\lambda^2}}} + \sum_{i=1}^{\infty} \alpha_i e^{-D\,k_i^2 t}\, {}_1F_1\Big(-\frac{\lambda^2 k_i^2}{2}; 1; \frac{r^2}{2\lambda^2} \Big) \right\}, \tag{B.26}$$

where

$$\alpha_i = \frac{R^2\, {}_1F_1\Big(-\frac{\lambda^2 k_i^2}{2}; 2; \frac{R^2}{2\lambda^2} \Big) - R_0^2\, {}_1F_1\Big(-\frac{\lambda^2 k_i^2}{2}; 2; \frac{R_0^2}{2\lambda^2} \Big)}{\int_0^R r'\, e^{-\frac{r'^2}{2\lambda^2}} \Big[{}_1F_1\Big(-\frac{\lambda^2 k_i^2}{2}; 1; \frac{r'^2}{2\lambda^2} \Big) \Big]^2 \mathrm{d}r'}. \tag{B.27}$$

As $R_0 \to 0$ in Eq. B.26 we recover Eq. B.24. Fig. B.7B shows traces of the concentration profile at the same times as in Fig. B.7A. Here, $R_0 = \frac{R}{2}$. Once again, we see that the analytical solution for $t = 0$ fluctuates about the defined initial condition but quickly smooth out and agree well with FEM results (hollow points) for $t > 0$. By removing molecules at $r \leq R_0$, a wave of molecules move toward the origin from a combination of advection toward the origin and diffusion moving molecules against the concentration gradient while the concentration at $r \to R$ recedes. Once again, we recover a Gaussian profile, but at a lower maximum than that observed in Fig. B.7A due to the lower initial number of molecules.

B.9.3 Gaussian profile for $r > R_0$

Finally, consider a situation where molecules in this advective-diffusive system are allowed to reach steady-state before photobleaching all molecules within a certain radius of the center $r \leq R_0$. The initial conditions would appear as

$$c(r,0) = \begin{cases} 0 & \text{if } r \leq R_0, \\ c_0\, e^{-\frac{r^2}{2\lambda^2}} & \text{if } r > R_0. \end{cases} \tag{B.28}$$

We show analytically that the concentration profile is

$$c(r,t) = c_0 e^{-\frac{r^2}{2\lambda^2}} \Bigg\{ \frac{e^{-\frac{R_0^2}{2\lambda^2}} - e^{-\frac{R^2}{2\lambda^2}}}{1 - e^{-\frac{R^2}{2\lambda^2}}} - \frac{1}{2} \sum_{i=1}^{\infty} \beta_i e^{-Dk_i^2 t}\, {}_1F_1\Big(-\frac{\lambda^2 k_i^2}{2}; 1; \frac{r^2}{2\lambda^2} \Big) \Bigg\}, \tag{B.29}$$

where

$$\beta_i = \frac{R_0^2\, {}_1F_1\Big(1 + \frac{\lambda^2 k_i^2}{2}; 2; -\frac{R_0^2}{2\lambda^2}\Big)}{\int_0^R r'\, e^{-\frac{r'^2}{2\lambda^2}} \Big[{}_1F_1\Big(-\frac{\lambda^2 k_i^2}{2}; 1; \frac{r'^2}{2\lambda^2} \Big) \Big]^2 \mathrm{d}r'}. \tag{B.30}$$

Once again the analytical solution agrees with simulations of the same initial condition shown in Fig. B.7C for $R_0 = \frac{R}{4}$. We note here that as $R_0 \to 0$ we recover the steady-state solution again as the time-dependent terms vanish and the ratio of exponentials in the time-independent term goes to unity. Fig. B.7C shows again the imperfection of the analytical solution for $t = 0$ and the initial condition but a strong agreement with FEM results. In this situation, the concentration toward the outer edge of the system remains largely unchanged as diffusion and advection are balanced toward the boundary. However, at smaller radii of the system, there is a shift in concentration as molecules enter the $r \leq R_0$ region and for the chosen parameter values, the overall concentration profile returns to a Gaussian distribution within 3 minutes.

Across all three initial conditions, the trend toward a Gaussian distribution as the steady-state profile shows that in experimental systems exhibiting such an advective-diffusive behavior the use of FRAP becomes sensitive to the time when photobleaching is applied. If the concentration profile in the system has already begun to move away from a uniform distribution, such as the initial contraction of a highly connected filament network, then the molecule

redistribution until steady state is achieved will show different recovery profiles from that of an experiment where photobleaching is applied at a time when the system is already close to reaching the steady-state profile. Such results provide the two extremes of "fluorescence recovery" in potential *in vitro* assays that evolve from a uniform concentration to a Gaussian-shaped distribution subject to this advection-diffusion system.

B.10 1D telescoping model

In this work, we present a theory for the redistribution of particles influenced by diffusion and advection with a linear velocity profile directed toward the origin. This theoretical analysis is meant to explore the filament concentration when subject to a linear contraction velocity profile. We start by illustrating this in a 1D system of length L. The velocity as a function of position is described by

$$v(x) = -v_{\mathrm{m}}\frac{x}{L},\ 0 \le x \le L, \tag{B.31}$$

where v_{m} is the maximum particle velocity in this system, located at $x = L$. We also note that the velocity is negative to indicate that the particles are moving toward $x = 0$. The general one-dimensional advection-diffusion equation says that the concentration changes in space and time $c(x,t)$ in the form

$$\frac{\partial c}{\partial t} = D\frac{\partial^2 c}{\partial x^2} - \frac{\partial}{\partial x}\Big[v(x)\,c\Big], \tag{B.32}$$

for D the diffusion constant. With a linear velocity profile, Eq. B.32 takes the form

$$\begin{aligned}\frac{\partial c}{\partial t} &= D\frac{\partial^2 c}{\partial x^2} + \frac{\partial}{\partial x}\Big(v_{\mathrm{m}}\frac{x}{L}c\Big),\\ &= D\frac{\partial^2 c}{\partial x^2} + \frac{v_{\mathrm{m}}\,x}{L}\frac{\partial c}{\partial x} + \frac{v_{\mathrm{m}}}{L}c.\end{aligned} \tag{B.33}$$

To solve Eq. B.33, we apply a separation of variables where our ansatz for the concentration of particles is

$$c(x,t) = \Phi(x)T(t). \tag{B.34}$$

We apply Eq. B.34 to Eq. B.33 and divide by $D\Phi(x)T(t)$ to get

$$\frac{1}{DT}\frac{\mathrm{d}T}{\mathrm{d}t} = \frac{1}{\Phi}\frac{\mathrm{d}^2\Phi}{\mathrm{d}x^2} + \frac{v_\mathrm{m}x}{DL}\frac{1}{\Phi}\frac{\mathrm{d}\Phi}{\mathrm{d}x} + \frac{v_\mathrm{m}}{DL}. \tag{B.35}$$

Due to the left-hand and right-hand sides of the equation depending only on t and x, respectively, we can say that both sides of Eq. B.35 are the same constant $-k^2$. We then solve the left-hand side of Eq. B.35:

$$\begin{aligned}\frac{1}{DT}\frac{\mathrm{d}T}{\mathrm{d}t} &= -k^2,\\ T(t) &= e^{-Dk^2t}.\end{aligned} \tag{B.36}$$

We are left to solve the right-hand side of Eq. B.35. Here, we get

$$\begin{aligned}-k^2 &= \frac{1}{\Phi}\frac{\mathrm{d}^2\Phi}{\mathrm{d}x^2} + \frac{v_\mathrm{m}x}{DL}\frac{1}{\Phi}\frac{\mathrm{d}\Phi}{\mathrm{d}x} + \frac{v_m}{DL},\\ 0 &= \frac{\mathrm{d}^2\Phi}{\mathrm{d}x^2} + \frac{v_\mathrm{m}\,x}{DL}\frac{\mathrm{d}\Phi}{\mathrm{d}x} + \Phi\Big[\frac{v_\mathrm{m}}{DL} + k^2\Big].\end{aligned} \tag{B.37}$$

We define a parameter $\alpha^2 = \frac{v_\mathrm{m}}{DL}$. When implemented into Eq. B.37, we get

$$\begin{aligned}0 &= \frac{\mathrm{d}^2\Phi}{\mathrm{d}x^2} + \alpha^2 x\frac{\mathrm{d}\Phi}{\mathrm{d}x} + \Phi\Big[\alpha^2 + k^2\Big],\\ 0 &= \frac{1}{\alpha^2}\frac{\mathrm{d}^2\Phi}{\mathrm{d}x^2} + x\frac{\mathrm{d}\Phi}{\mathrm{d}x} + \Phi\Big[1 + \Big(\frac{k}{\alpha}\Big)^2\Big],\\ &= \frac{\mathrm{d}^2\Phi}{\mathrm{d}\tilde{x}^2} + \tilde{x}\frac{\mathrm{d}\Phi}{\mathrm{d}\tilde{x}} + \Phi\Big(1 + \tilde{k}^2\Big),\end{aligned} \tag{B.38}$$

where we redefined $\tilde{x} = \alpha x$ and $\tilde{k} = \frac{k}{\alpha}$.

In order to solve for Φ, we applied the ODE into Wolfram Alpha. The general solution takes the form

$$\Phi(\tilde{x}) = c_\mathrm{ss}\, e^{-\frac{\tilde{x}^2}{2}} + c_1\, e^{-\frac{\tilde{x}^2}{2}} H_{\tilde{k}^2}\Big(\frac{\tilde{x}}{\sqrt{2}}\Big) + c_2\, e^{-\frac{\tilde{x}^2}{2}}\, {}_1F_1\Big(-\frac{\tilde{k}^2}{2}; \frac{1}{2}; \frac{\tilde{x}^2}{2}\Big), \tag{B.39}$$

where $H_n(x)$ is the nth Hermite polynomial and ${}_1F_1(a;b;z)$ is the Kummer confluent hypergeometric function. When we apply no-flux boundary conditions to the problem, we are looking to satisfy the conditions $J_x|_{x=0} = 0$ and

$J_x|_{x=L} = 0$. We note that $J_x = D\frac{\mathrm{d}\Phi}{\mathrm{d}x} - v(x)\Phi(x)$ rather than simply $\frac{\mathrm{d}\Phi}{\mathrm{d}x} = 0$ at the boundaries where the advection of material coming in must be countered by diffusion going outward to ensure that the number of particles is constant in the system.

Fortunately, both boundary conditions are satisfied for the steady-state solution. However, when we apply these conditions to the Hermite polynomials, the condition at $x = 0$ requires that $\tilde{k}^2$ be an even integer, but the boundary condition at $x = L$ requires that

$$H'_{2n}\Big(\frac{\alpha\, L}{\sqrt{2}}\Big) = 0. \tag{B.40}$$

To be able to satisfy this boundary condition, we would have to ensure that the derivative of each even function of the Hermite polynomial is 0 at $\frac{\alpha\, L}{\sqrt{2}}$. However, as L, v_m, and D are defined properties of the system, we are left to argue that the coefficients of the Hermite polynomials are 0. Finally, we check that the Kummer confluent hypergeometric function can satisfy our boundary conditions. We start with $x = 0$:

$$\begin{aligned}
\frac{\mathrm{d}\Phi}{\mathrm{d}x}\Big|_{x=0} &= 0,\\
c_2\frac{\mathrm{d}\tilde{x}}{\mathrm{d}x}\frac{\mathrm{d}}{\mathrm{d}\tilde{x}}\Big[e^{-\frac{\tilde{x}^2}{2}}{}_1F_1\Big(-\frac{\tilde{k}^2}{2};\frac{1}{2};\frac{\tilde{x}^2}{2}\Big)\Big] &= 0,\\
c_2\,\alpha\, e^{-\frac{\tilde{x}^2}{2}}\Big[-\tilde{x}\,{}_1F_1\Big(-\frac{\tilde{k}^2}{2};\frac{1}{2};\frac{\tilde{x}^2}{2}\Big) + \sum_{l=1}^{\infty}\tilde{x}\frac{\Big(-\frac{\tilde{k}^2}{2}\Big)_l}{\Big(\frac{1}{2}\Big)_l}\frac{\Big(\frac{\tilde{x}^2}{2}\Big)^{l-1}}{(l-1)!}\Big] &= 0,\\
0 &= 0.
\end{aligned} \tag{B.41}$$

Eq. B.41 shows that all terms of the function for Φ will satisfy the boundary conditions without a need to specify $\tilde{k}$. Applying the boundary condition at $x = L$ gives:

$${}_1F_1\Big(1-\frac{\tilde{k}^2}{2};\frac{3}{2};\frac{(\alpha L)^2}{2}\Big) = 0. \tag{B.42}$$

In order to get to this solution, we used the case that $(a)_l = (a)(a+1)(a+2)...(a+l-1) = a\,(a+1)_{l-1}$ so that we return to a Hypergeometric function. In essence, we then need to solve for $\tilde{k}$ through Eq. B.42 in order to obtain each value of k in our original problem.

Fig. B.8 plots the left-hand side of Eq. B.42 as a function of $\tilde{k}$ when $\alpha L = 1$. That is, for simplicity, we set all of the parameters of the system to unity. In

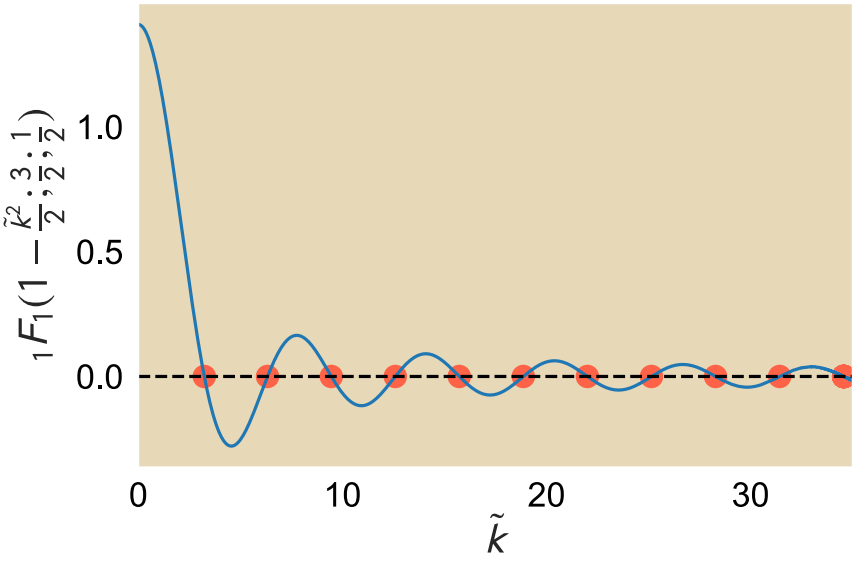

Figure B.8: **Zeros of $\tilde{k}$ for $_1F_1\Big(1-\frac{\tilde{k}^2}{2};\frac{3}{2};\frac{(\alpha L)^2}{2}\Big)=0$ where $\alpha L=1$.** Red dots are overlayed with the points where the Kummer confluent hypergeometric function crosses the x-axis.

this case, we can see a roughly periodic nature to the hypergeometric function. The first five solutions for $\tilde{k}$ are $\tilde{k}=3.231$, 6.329, 9.456, 12.589, and 15.727, which we will refer to later.

So far, the solution to Eq. B.33 with no-flux boundary conditions is

$$c(x,t)=c_{\mathrm{ss}}\exp\Big(-\frac{v_{\mathrm{m}}x^2}{2\,D\,L}\Big) + \sum_{j=1}^{\infty}c_j\exp\Big(-Dk_j^2t-\frac{v_{\mathrm{m}}x^2}{2DL}\Big)\,{}_1F_1\Big(-\frac{DLk_j^2}{2v_{\mathrm{m}}};\frac{1}{2};\frac{v_{\mathrm{m}}x^2}{2DL}\Big), \quad \text{(B.43)}$$

where k_j is determined from finding the values of $\tilde{k}_j\equiv\frac{k_j}{\alpha}$ for which $_1F_1\Big(1-\frac{\tilde{k}^2}{2};\frac{3}{2};\frac{(\alpha L)^2}{2}\Big)=0$. In the case where we set $L=1$, $D=1$, and $v_{\mathrm{m}}=1$, we are solving

$$c(x,t)=c_{\mathrm{ss}}\exp\Big(-\frac{x^2}{2}\Big)+\sum_{j=1}^{\infty}c_j\exp\Big(-k_j^2t-\frac{x^2}{2}\Big)\,{}_1F_1\Big(-\frac{k_j^2}{2};\frac{1}{2};\frac{x^2}{2}\Big), \quad \text{(B.44)}$$

$$_1F_1\Big(1-\frac{k_j^2}{2};\frac{3}{2};\frac{1}{2}\Big)=0.$$

Here, we have determined the first few values of k_j that satisfy the no-flux boundary condition. We now find the coefficients $\{c_j\}$ from solving the initial

condition. There are many possible initial conditions we could consider, but suppose we let a one-dimensional aster assay carry out to form a steady-state aster. At $t < 0$, the concentration of fluorescent molecules in the system is the steady-state concentration profile $c_{\text{ss}}\, e^{-\frac{x^2}{2}}$, but then we photobleach the molecules at positions $x < x_0 < 1$. In this case, our initial conditions appear as

$$c(x,0) = \begin{cases} 0 & \text{if } x \le x_0, \\ c_0\, e^{-\frac{x^2}{2}} & \text{if } x > x_0. \end{cases} \tag{B.45}$$

In order to solve the initial conditions, we must multiply both sides of Eq. B.43 by an eigenfunction with some value of k_h that satisfies the boundary conditions, $e^{-\frac{x^2}{2}}\, {}_1F_1\Big(-\frac{k_h^2}{2}; \frac{1}{2}; \frac{x^2}{2}\Big)$. We also use the weighting function $w(x) = e^{\frac{x^2}{2}}$ as derived in Appendix B.11:

$$\begin{aligned} \int_0^1 c(x,0)\, w(x)\, e^{-\frac{x^2}{2}}\, {}_1F_1\Big(-\frac{k_h^2}{2}; \frac{1}{2}; \frac{x^2}{2}\Big)\, \mathrm{d}x &= c_{\text{ss}} \int_0^1 e^{-\frac{x^2}{2}}\, {}_1F_1\Big(-\frac{k_h^2}{2}; \frac{1}{2}; \frac{x^2}{2}\Big)\, \mathrm{d}x \\ &\quad + \Bigg[\sum_{j=1}^{\infty} c_j \int_0^1 e^{-\frac{x^2}{2}}\, {}_1F_1\Big(-\frac{k_j^2}{2}; \frac{1}{2}; \frac{x^2}{2}\Big) \\ &\quad \times {}_1F_1\Big(-\frac{k_h^2}{2}; \frac{1}{2}; \frac{x^2}{2}\Big)\mathrm{d}x\Bigg], \\ c_0 \int_{x_0}^1 e^{-\frac{x^2}{2}}\, {}_1F_1\Big(-\frac{k_h^2}{2}; \frac{1}{2}; \frac{x^2}{2}\Big)\, \mathrm{d}x &= c_{\text{ss}} \int_0^1 e^{-\frac{x^2}{2}}\, {}_1F_1\Big(-\frac{k_h^2}{2}; \frac{1}{2}; \frac{x^2}{2}\Big)\, \mathrm{d}x \\ &\quad + \Bigg[\sum_{j=1}^{\infty} c_j \int_0^1 e^{-\frac{x^2}{2}}\, {}_1F_1\Big(-\frac{k_j^2}{2}; \frac{1}{2}; \frac{x^2}{2}\Big) \\ &\quad \times {}_1F_1\Big(-\frac{k_h^2}{2}; \frac{1}{2}; \frac{x^2}{2}\Big)\mathrm{d}x\Bigg]. \end{aligned} \tag{B.46}$$

We first tackle the left-hand side of Eq. B.46. By invoking a relation for Kummer confluent hypergeometric functions of the first kind:

$${}_1F_1\Big(a; b; x\Big) = e^x\, {}_1F_1\Big(b-a; b; -x\Big), \tag{B.47}$$

the integral can be altered to take the form

$$c_0 \int_{x_0}^{1} e^{-\frac{x^2}{2}}\, {}_1F_1\Big(-\frac{k_h^2}{2}; \frac{1}{2}; \frac{x^2}{2}\Big)\,\mathrm{d}x = c_0 \int_{x_0}^{1} {}_1F_1\Big(\frac{1+k_h^2}{2}; \frac{1}{2}; -\frac{x^2}{2}\Big)\,\mathrm{d}x,$$
$$= c_0 \frac{x}{2} \sum_{i=0}^{\infty} \frac{\Big(\frac{1}{2}+\frac{k_h^2}{2}\Big)_i}{\Big(\frac{1}{2}\Big)_i \Big(i+\frac{1}{2}\Big)} \frac{\Big(-\frac{x^2}{2}\Big)^i}{i!}\Bigg|_{x_0}^{1}, \quad \text{(B.48)}$$

and by using $(a)_i(a+i) = a(a+1)...(a+i-1)(a+i) = a(a+1)_i$, and using Eq. B.47 we get

$$c_0 \int_{x_0}^{1} e^{-\frac{x^2}{2}}\, {}_1F_1\Big(-\frac{k_h^2}{2}; \frac{1}{2}; \frac{x^2}{2}\Big)\,\mathrm{d}x = c_0 \frac{x}{2\frac{1}{2}} \sum_{i=0}^{\infty} \frac{\Big(\frac{1}{2}+\frac{k_h^2}{2}\Big)_i}{\Big(\frac{3}{2}\Big)_i} \frac{\Big(-\frac{x^2}{2}\Big)^i}{i!}\Bigg|_{x_0}^{1},$$
$$= c_0\, x\, {}_1F_1\Big(\frac{1}{2}+\frac{k_h^2}{2}; \frac{3}{2}; -\frac{x^2}{2}\Big)\Bigg|_{x_0}^{1},$$
$$= c_0\, x\, e^{-\frac{x^2}{2}}\, {}_1F_1\Big(1-\frac{k_h^2}{2}; \frac{3}{2}; \frac{x^2}{2}\Big)\Bigg|_{x_0}^{1},$$
$$= c_0 \Big[e^{-\frac{1}{2}}\, {}_1F_1\Big(1-\frac{k_h^2}{2}; \frac{3}{2}; \frac{1}{2}\Big)$$
$$- x_0\, e^{-\frac{x_0^2}{2}}\, {}_1F_1\Big(1-\frac{k_h^2}{2}; \frac{3}{2}; \frac{x_0^2}{2}\Big)\Big],$$
$$= -c_0\, x_0 e^{-\frac{x_0^2}{2}}\, {}_1F_1\Big(1-\frac{k_h^2}{2}; \frac{3}{2}; \frac{x_0^2}{2}\Big). \quad \text{(B.49)}$$

Where the first term in the penultimate line is 0 due to Eq. B.42.

Integrating the term with the steady-state solution simply leads to an integral of the hypergeometric function:

$$\int_0^1 e^{-\frac{x^2}{2}}\, {}_1F_1\Big(-\frac{k_h^2}{2}; \frac{1}{2}; \frac{x^2}{2}\Big)\mathrm{d}x = e^{-\frac{1}{2}}\, {}_1F_1\Big(1-\frac{k_h^2}{2}; \frac{3}{2}; \frac{1}{2}\Big),$$
$$= 0. \quad \text{(B.50)}$$

So the first integral on the right-hand side vanishes. This makes sense as the steady-state function, being an eigenfunction of the PDE is orthogonal to the eigenfunction chosen.

Finally, we solve for the second integral on the right-hand side. We showed in Eq. B.66 of Sec. B.11 that for $j \neq h$, the integral is 0. This leaves only

one integral to tackle, where $j = h$. For this problem, this integral must be performed numerically. The coefficients are then solved as

$$c_h = -c_0 \frac{x_0 e^{-\frac{x_0^2}{2}}\, {}_1F_1\Big(1 - \frac{k_h^2}{2}; \frac{3}{2}; \frac{x_0^2}{2}\Big)}{\int_0^1 e^{-\frac{x^2}{2}} \Big[{}_1F_1\Big(-\frac{k_h^2}{2}; \frac{1}{2}; \frac{x^2}{2}\Big)\Big]^2 \mathrm{d}x}. \tag{B.51}$$

Finally, we determine the coefficient for the steady-state solution. To achieve this, we multiply both sides by the weighting function $w(x)$ and the steady-state eigenfunction as prescribed in Eq. B.62 of Sec. B.11. In this case, the product of the two functions cancel, so we integrate each side over the system size:

$$\begin{aligned} c_0 \int_{x_0}^1 e^{-\frac{x^2}{2}}\, \mathrm{d}x &= c_{\mathrm{ss}} \int_0^1 e^{-\frac{x^2}{2}} \mathrm{d}x + \sum_{j=1}^{\infty} c_j \int_0^1 e^{-\frac{x^2}{2}}\, {}_1F_1\Big(-\frac{k_j^2}{2}; \frac{1}{2}; \frac{x^2}{2}\Big)\mathrm{d}x, \\ c_0 \sqrt{\frac{\pi}{2}} \mathrm{erf}\Big(\frac{x}{\sqrt{2}}\Big)\Big|_{x_0}^1 &= c_{\mathrm{ss}} \sqrt{\frac{\pi}{2}} \mathrm{erf}\Big(\frac{x}{\sqrt{2}}\Big)\Big|_0^1, \\ c_{\mathrm{ss}} &= c_0 \left[1 - \frac{\mathrm{erf}\Big(\frac{x_0}{\sqrt{2}}\Big)}{\mathrm{erf}\Big(\frac{1}{\sqrt{2}}\Big)}\right], \end{aligned} \tag{B.52}$$

where $\mathrm{erf}(x)$ is the Gauss error function and the integrals with the hypergeometric functions vanish as demonstrated from Eq. B.50. When we assemble all of the terms for this particular initial condition and reintroduce the parameters, the solution takes the form

$$\begin{aligned} c(x,t) = c_0\, e^{-\frac{v_{\mathrm{m}} x^2}{2DL}} \Bigg\{ 1 - \frac{\mathrm{erf}\Big(x_0 \sqrt{\frac{v_{\mathrm{m}}}{2DL}}\Big)}{\mathrm{erf}\Big(\sqrt{\frac{v_{\mathrm{m}} L}{2D}}\Big)} \\ - \sum_{j=1}^{\infty} \frac{x_0 e^{-\frac{v_{\mathrm{m}} x_0^2}{2DL}}\, {}_1F_1\Big(1 - \frac{DLk_j^2}{2v_{\mathrm{m}}}; \frac{3}{2}; \frac{v_{\mathrm{m}} x_0^2}{2DL}\Big)}{\int_0^L e^{-\frac{v_{\mathrm{m}} x^2}{2DL}} \Big[{}_1F_1\Big(-\frac{DLk_j^2}{2v_{\mathrm{m}}}; \frac{1}{2}; \frac{x^2}{2}\Big)\Big]^2 \mathrm{d}x} e^{-Dk_j^2 t}\, {}_1F_1\Big(-\frac{DLk_j^2}{2v_{\mathrm{m}}}; \frac{1}{2}; \frac{v_{\mathrm{m}} x^2}{2DL}\Big) \Bigg\}. \end{aligned} \tag{B.53}$$

Fig. B.9A illustrates the initial Gaussian profile (red dashed line) prior to photobleaching from $x < x_0$ (solid black line). Fig. B.9B shows the FRAP recovery process at various time units as solved in Eq. B.53. We observe that the increase in concentration toward $x = 0$ and the decrease in concentration toward $x = L = 1$ appear to generally match one another over the course of the recover. We also see that by $t = 0.500$, we have returned to a Gaussian profile as the steady-state profile, but with a reduced peak concentration.

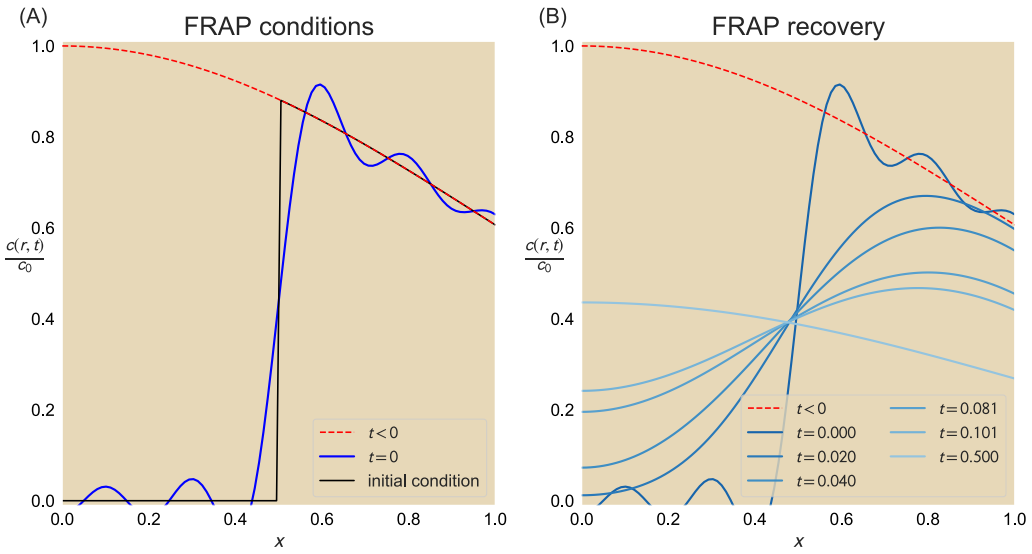

Figure B.9: **FRAP for 1D advection diffusion with linear velocity profile.** (A) Initial steady-state profile of the concentration (red dashed line) before photobleaching the system for $x < x_0$ (solid black line). The blue line is obtained from Eq. B.53 for the first nonzero values of k_j for the given problem. (B) Time evolution of the concentration after photobleaching. Decreasing shades of blue designate later time points of the concentration profile.

B.11 Sturm-Liouville Theory

The Sturm-Liouville theory says that all second-order linear ordinary differential equations can be written in the form

$$\frac{\mathrm{d}}{\mathrm{d}x}\Big[p(x)\frac{\mathrm{d}y}{\mathrm{d}x}\Big] + q(x)\,y(x) = -\lambda\,w(x)\,y(x). \tag{B.54}$$

Importantly, $w(x)$ is the weighting function, which provides the means for satisfying the orthogonality relations for finding coefficients of each term in the series solution to the partial differential equation. Specifically, if we were to write the ODE in the form

$$P(x)\,y''(x) + Q(x)\,y'(x) + R(x)\,y(x) = f(x), \tag{B.55}$$

for functions $P(x)$, $Q(x)$, $R(x)$, and $f(x)$, then there is a multiplicative function that can be determined by

$$m(x) = \exp\Big(\int \frac{Q(x) - P'(x)}{P(x)}\mathrm{d}x\Big). \tag{B.56}$$

This multiplicative function is then multiplied to Eq. B.55 and recast into the form shown in Eq.B.54. Thus, with $P(\tilde{x}) = 1$ and $Q(\tilde{x}) = \tilde{x}$,

$$\begin{aligned} m(\tilde{x}) &= \exp\Big(\int \tilde{x}\,\mathrm{d}\tilde{x}\Big), \\ &= \exp\Big(\frac{\tilde{x}^2}{2}\Big), \end{aligned} \tag{B.57}$$

and the ODE takes the form

$$0 = \frac{\mathrm{d}}{\mathrm{d}\tilde{x}}\Big[e^{\frac{\tilde{x}^2}{2}}\frac{\mathrm{d}\Phi}{\mathrm{d}\tilde{x}}\Big] + \Phi\Big(1+\tilde{k}^2\Big)e^{\frac{\tilde{x}^2}{2}}, \tag{B.58}$$

or in the form of Eq. B.54:

$$\frac{\mathrm{d}}{\mathrm{d}\tilde{x}}\Big[e^{\frac{\tilde{x}^2}{2}}\frac{\mathrm{d}\Phi}{\mathrm{d}\tilde{x}}\Big] + e^{\frac{\tilde{x}^2}{2}}\Phi = -\tilde{k}^2 e^{\frac{\tilde{x}^2}{2}}\Phi, \tag{B.59}$$

so that $p(x) = q(x) = w(x) = e^{\frac{\tilde{x}^2}{2}}$ and $\lambda = \tilde{k}^2$. We note the weighting function here is the same as the multiplicative function for the 1D advection-diffusion equation reported here.

Next, we show the orthogonality conditions of the eigenfunctions. Suppose that solving Eq. B.54 creates a series of eigenfunctions $\{y_j(x)\}$. Suppose that a given eigenfunction $y_i(x)$ has the eigenvalue λ_i so that

$$\frac{\mathrm{d}}{\mathrm{d}x}\Big[p(x)\frac{\mathrm{d}y_i}{\mathrm{d}x}\Big] + q(x)\,y_i(x) = -\lambda_i\,w(x)\,y_i(x). \tag{B.60}$$

Suppose that each eigenfunction of the system, bounded by $a \le x \le b$, obeys the boundary conditions

$$\begin{aligned} \alpha_1 y_i(a) + \alpha_2 y_i'(a) &= 0, \\ \beta_1 y_i(b) + \beta_2 y_i'(b) &= 0. \end{aligned} \tag{B.61}$$

To test the orthogonality conditions, we multiply both sides by $y_j(x)$, a particular eigenfunction of the differential equation, and integrate over the entire system:

$$\int_a^b \frac{\mathrm{d}}{\mathrm{d}x}\Big[p(x)\frac{\mathrm{d}y_i}{\mathrm{d}x}\Big]y_j(x) + q(x)\,y_i(x)\,y_j(x)\mathrm{d}x = -\lambda_i \int_a^b w(x)\,y_i(x)\,y_j(x)\mathrm{d}x,$$
$$p(x)\frac{\mathrm{d}y_i}{\mathrm{d}x}y_j(x)\Big|_a^b - \int_a^b p(x)\frac{\mathrm{d}y_i}{\mathrm{d}x}\frac{\mathrm{d}y_j}{\mathrm{d}x}\mathrm{d}x + \int_a^b q(x)\,y_i(x)\,y_j(x)\mathrm{d}x = -\lambda_i \int_a^b w(x)\,y_i(x)\,y_j(x)\mathrm{d}x. \tag{B.62}$$

Had Eq. B.60 involved $y_j(x)$ and we multiplied both sides of the equation by $y_i(x)$, then Eq. B.62 would have the subscripts reversed:

$$p(x)\frac{\mathrm{d}y_j}{\mathrm{d}x}y_i(x)\Big|_a^b - \int_a^b p(x)\frac{\mathrm{d}y_i}{\mathrm{d}x}\frac{\mathrm{d}y_j}{\mathrm{d}x}\mathrm{d}x + \int_a^b q(x)\,y_i(x)\,y_j(x)\mathrm{d}x = -\lambda_j \int_a^b w(x)\,y_i(x)\,y_j(x)\mathrm{d}x. \tag{B.63}$$

Suppose we subtracted Eq. B.63 from Eq. B.62 and applied our boundary conditions:

$$\begin{aligned}
-(\lambda_i-\lambda_j)\int_a^b w(x)\,y_i(x)\,y_j(x)\mathrm{d}x &= p(x)\frac{\mathrm{d}y_i}{\mathrm{d}x}y_j(x)\Big|_a^b - p(x)\frac{\mathrm{d}y_i}{\mathrm{d}x}y_j(x)\Big|_a^b,\\
-(\lambda_i-\lambda_j)\int_a^b w(x)\,y_i(x)\,y_j(x)\mathrm{d}x &= p(b)\Big[\frac{\mathrm{d}y_i}{\mathrm{d}x}\Big|_b y_j(b) - \frac{\mathrm{d}y_j}{\mathrm{d}x}\Big|_b y_i(b)\Big]\\
&\quad - p(a)\Big[\frac{\mathrm{d}y_i}{\mathrm{d}x}\Big|_a y_j(a) - \frac{\mathrm{d}y_j}{\mathrm{d}x}\Big|_a y_i(a)\Big],\\
-(\lambda_i-\lambda_j)\int_a^b w(x)\,y_i(x)\,y_j(x)\mathrm{d}x &= p(b)\Big[\frac{\beta_1}{\beta_2}y_i(b)\,y_j(b) - \frac{\beta_1}{\beta_2}y_i(b)\,y_j(b)\Big]\\
&\quad - p(a)\Big[\frac{\alpha_1}{\alpha_2}y_i(a)\,y_j(a) - \frac{\alpha_1}{\alpha_2}y_i(a)\,y_j(a)\Big],\\
-(\lambda_i-\lambda_j)\int_a^b w(x)\,y_i(x)\,y_j(x)\mathrm{d}x &= 0.
\end{aligned} \tag{B.64}$$

If $i = j$, then the left-hand side is already zero.

$$-\lambda_i \int_a^b w(x)\Big[y_i(x)\Big]^2\mathrm{d}x = p(x)\frac{\mathrm{d}y_i}{\mathrm{d}x}y_i(x)\Big|_a^b - \int_a^b p(x)\Big[\frac{\mathrm{d}y_i}{\mathrm{d}x}\Big]^2\mathrm{d}x + \int_a^b q(x)\Big[y_i(x)\Big]^2\mathrm{d}x. \tag{B.65}$$

We will return to the case where $i = j$ to find the coefficients of eigenfunction. If $i \neq j$, then the eigenvalues are different here and the integral is zero:

$$\int_a^b w(x)\, y_i(x)\, y_j(x)\mathrm{d}x = 0, \text{for } i \neq j. \tag{B.66}$$

Though not true for the 1D case, Eq. B.65 may serve as a convenient equation for analytically solving the coefficients for each eigenfunction.

B.12 2D telescoping model

In the 2D telescoping case, we assume that we are carrying out an aster assay experiment where we dimerize motors (and thus couple microtubules) in a circular region of radius R. We assume that the distributions of motors and microtubules are strictly radially dependent and thus have no angular dependence. Finally, we model the velocity profile of the microtubule movement by assuming radially inward advection of particles where those that lie further away from the origin move faster than those toward the center:

$$\mathbf{v} = -v_\mathrm{m}\frac{r}{R}\hat{r}. \tag{B.67}$$

The advection-diffusion equation then takes the form

$$\begin{aligned}
\frac{\partial c}{\partial t} &= D\nabla^2 c - \nabla\cdot(\mathbf{v}c), \\
&= \frac{D}{r}\frac{\partial}{\partial r}\Big(r\frac{\partial c}{\partial r}\Big) + \frac{v_\mathrm{m}}{R}\frac{1}{r}\frac{\partial}{\partial r}(r^2 c), \\
&= D\frac{\partial^2 c}{\partial r^2} + \frac{D}{r}\frac{\partial c}{\partial r} + \frac{v_\mathrm{m} r}{R}\frac{\partial c}{\partial r} + \frac{2v_\mathrm{m}c}{R}, \\
&= D\frac{\partial^2 c}{\partial r^2} + \Big(\frac{D}{r} + \frac{v_\mathrm{m} r}{R}\Big)\frac{\partial c}{\partial r} + \frac{2v_\mathrm{m}c}{R}, \\
\frac{1}{D}\frac{\partial c}{\partial t} &= \frac{\partial^2 c}{\partial r^2} + \Big(\frac{1}{r} + \frac{v_\mathrm{m} r}{DR}\Big)\frac{\partial c}{\partial r} + \frac{2v_\mathrm{m}c}{DR}.
\end{aligned} \tag{B.68}$$

We first follow the procedure of separation of variables $c(r,t) = \Phi(r)T(t)$ and determine that the time-dependent component takes on the familiar form of $e^{-Dk^2 t}$. This ansatz is then applied to Eq. B.68 and rewrite the spatial component of the concentration as

$$\begin{aligned}
-k^2\Phi &= \frac{\mathrm{d}^2\Phi}{\mathrm{d}r^2} + \Big(\frac{1}{r} + \frac{v_\mathrm{m} r}{DR}\Big)\frac{\mathrm{d}\Phi}{\mathrm{d}r} + \frac{2v_\mathrm{m}\Phi}{DR}, \\
0 &= r\frac{\mathrm{d}^2\Phi}{\mathrm{d}r^2} + \Big(1 + \frac{v_\mathrm{m} r^2}{DR}\Big)\frac{\mathrm{d}\Phi}{\mathrm{d}r} + \Big(\frac{2v_\mathrm{m}}{DR} + k^2\Big)r\Phi.
\end{aligned} \tag{B.69}$$

We will define a new length scale $\lambda^2 \equiv \frac{DR}{v_\mathrm{m}}$ as well as a change of variables $\rho \equiv \frac{r}{\lambda}$ and $\tilde{k} \equiv \lambda k$. In this case, Eq. B.69 takes the altered form

$$0 = \rho\frac{\mathrm{d}^2\Phi}{\mathrm{d}\rho^2} + (1+\rho^2)\frac{\mathrm{d}\Phi}{\mathrm{d}\rho} + \Big(2 + \tilde{k}^2\Big)\rho\Phi. \tag{B.70}$$

We obtain the multiplicative function by following the prescription from Eq. B.56 in Sec. B.11:

$$m(\rho) = e^{\frac{\rho^2}{2}}. \tag{B.71}$$

When we multiply Eq. B.70 by the multiplicative function, we get

$$\begin{aligned} 0 &= \rho\, e^{\frac{\rho^2}{2}} \frac{\mathrm{d}^2\Phi}{\mathrm{d}\rho^2} + (1+\rho^2) e^{\frac{\rho^2}{2}} \frac{\mathrm{d}\Phi}{\mathrm{d}\rho} + \left(2 + \tilde{k}^2\right) \rho\, e^{\frac{\rho^2}{2}} \Phi, \\ \frac{\mathrm{d}}{\mathrm{d}\rho}\left[\rho\, e^{\frac{\rho^2}{2}} \frac{\mathrm{d}\Phi}{\mathrm{d}\rho}\right] &+ 2\rho\, e^{\frac{\rho^2}{2}} \Phi = -\tilde{k}^2 \rho\, e^{\frac{\rho^2}{2}} \Phi. \end{aligned} \tag{B.72}$$

Eq. B.72 shows that unlike the 1D advection-diffusion telescoping model, the weighting function differs from the multiplicative function due to the inclusion of the prefactor ρ. In this case, the weighting function $w(\rho)$ as well as $p(\rho)$ and $q(\rho)$ are given as

$$w(\rho) = p(\rho) = q(\rho) = \rho\, e^{\frac{\rho^2}{2}}. \tag{B.73}$$

Furthermore, we observe that, as in the 1D case, the eigenvalues take the form $\tilde{k}^2$. Solutions of Φ from Eq. B.72 are obtained from Wolfram Alpha and take the form

$$\begin{aligned} \Phi_{\mathrm{ss}}(\rho) &= c_{\mathrm{ss}}\, e^{-\frac{\rho^2}{2}}, \\ \Phi_{\mathrm{dyn}}(\rho) &= c_1\, e^{-\frac{\rho^2}{2}}\, {}_1F_1\left(-\frac{\tilde{k}^2}{2}; 1; \frac{\rho^2}{2}\right) + c_2\, G^{2,0}_{1,2}\left(\frac{\rho^2}{2}\middle| \begin{matrix} -\frac{\tilde{k}^2}{2} \\ 0, 0 \end{matrix}\right), \end{aligned} \tag{B.74}$$

where $G^{m,n}_{p,q}\left(z\middle| \begin{matrix} a_1,\ldots,a_p \\ b1,\ldots,b_q \end{matrix}\right)$ is the Meijer G-function (we split up the eigenfunctions as dynamic and steady-state terms for now). We note here that the arguments of the Meijer G-function are such that the function diverges at the origin. As our system is defined as $0 \leq r \leq R$, we can say that $c_2 = 0$. Thus, our eigenfunctions are

$$\begin{aligned} \Phi_{\mathrm{ss}}(\rho) &= c_{\mathrm{ss}}\, e^{-\frac{\rho^2}{2}}, \\ \Phi_{\mathrm{dyn}}(\rho) &= c_1\, e^{-\frac{\rho^2}{2}}\, {}_1F_1\left(-\frac{\tilde{k}^2}{2}; 1; \frac{\rho^2}{2}\right), \end{aligned} \tag{B.75}$$

where we note that in the case of $\tilde{k} = 0$, we go from the dynamic eigenfunction to the static eigenfunction.

B.12.1 No-flux boundary condition

In the work presented here, there is no inflow or outflow of material at the boundary. Thus, we impose the boundary condition $\mathbf{J}\Big|_{r=R} = 0$. This means that

$$J_r\Big|_{r=R} = D\frac{\mathrm{d}\Phi}{\mathrm{d}r} - v(R)\Phi(R) = D\frac{\mathrm{d}\Phi}{\mathrm{d}r}\Big|_{r=R} + v_\mathrm{m}\Phi(R) = 0. \tag{B.76}$$

We know that Eq. B.76 is satisfied for the steady-state eigenfunction in the same way that the 1D steady-state solution satisfied the boundary condition. We then need to ensure that the boundary condition is satisfied for the dynamic eigenfunction. We start by taking the derivative of the eigenfunction:

$$\begin{aligned}\frac{\mathrm{d}\Phi}{\mathrm{d}r} &= -\frac{c_1\,\rho}{\lambda}\,e^{-\frac{\rho^2}{2}}\Big[\frac{\tilde{k}^2}{2}{}_1F_1\Big(1-\frac{\tilde{k}^2}{2};2;\frac{\rho^2}{2}\Big) + {}_1F_1\Big(-\frac{\tilde{k}^2}{2};1;\frac{\rho^2}{2}\Big)\Big],\\ \frac{\mathrm{d}\Phi}{\mathrm{d}r}\Big|_{r=R} &= -\frac{c_1\,v_\mathrm{m}}{D}\,e^{-\frac{v_\mathrm{m}R}{2D}}\Big[\Big(\frac{DRk^2}{2v_\mathrm{m}}\Big){}_1F_1\Big(1-\frac{DRk^2}{2v_\mathrm{m}};2;\frac{v_\mathrm{m}R}{2D}\Big) + {}_1F_1\Big(-\frac{DRk^2}{2v_\mathrm{m}};1;\frac{v_\mathrm{m}R}{2D}\Big)\Big].\end{aligned} \tag{B.77}$$

so when applied to the boundary condition, we get

$$\begin{aligned}D\frac{\mathrm{d}\Phi}{\mathrm{d}r}\Big|_{r=R} + v_\mathrm{m}\Phi(R) = &-c_1\,v_\mathrm{m}\,e^{-\frac{v_\mathrm{m}R}{2D}}\Big(\frac{DRk^2}{2v_\mathrm{m}}\Big){}_1F_1\Big(1-\frac{DRk^2}{2v_\mathrm{m}};2;\frac{v_\mathrm{m}R}{2D}\Big)\\ &- c_1\,v_\mathrm{m}\,e^{-\frac{v_\mathrm{m}R}{2D}}{}_1F_1\Big(-\frac{DRk^2}{2v_\mathrm{m}};1;\frac{v_\mathrm{m}R}{2D}\Big)\\ &+ c_1\,v_\mathrm{m}\,e^{-\frac{v_\mathrm{m}R}{2D}}{}_1F_1\Big(-\frac{DRk^2}{2v_\mathrm{m}};1;\frac{v_\mathrm{m}R}{2D}\Big).\end{aligned} \tag{B.78}$$

We are then left with the simplified equation:

$$\Big(\frac{DRk^2}{2v_\mathrm{m}}\Big){}_1F_1\Big(1-\frac{DRk^2}{2v_\mathrm{m}};2;\frac{v_\mathrm{m}R}{2D}\Big) = 0. \tag{B.79}$$

Here, $k = 0$ is satisfied, which yields the steady-state solution. Fig. B.10 shows the zeros when we set $\frac{R}{\lambda} = 3.16$. The first few non-zero eigenvalues are then $\tilde{k} = 0.474$, 0.759, 1.058, 1.354, and 1.672. Here, we observe a similar oscillator pattern to the zeros of the system. Once again, we see that there are multiple values of k that satisfy the boundary conditions. This means that the solution to the advection-diffusion problem once both boundary and initial conditions are satisfied, is a superposition of the different eigenfunctions:

$$c(r,t) = c_\mathrm{ss}\,e^{-\frac{v_\mathrm{m}r^2}{2DR}} + e^{-\frac{v_\mathrm{m}r^2}{2DR}}\sum_{i=1}^{\infty} c_i e^{-Dk_i^2 t}\,{}_1F_1\Big(-\frac{DRk_i^2}{2v_\mathrm{m}};1;\frac{v_\mathrm{m}r^2}{2DR}\Big). \tag{B.80}$$

We emphasize here the parallel between Eq. B.43 in the 1D case and Eq. B.80 in the 2D case. The primary difference between the two equations is the second argument in the Kummer confluent hypergeometric function. For simplicity, we will reintroduce the length scale $\lambda \equiv \sqrt{\frac{DR}{v_m}}$ so that the equation is simplified as

$$c(r,t) = c_{ss}\, e^{-\frac{r^2}{2\lambda^2}} + e^{-\frac{r^2}{2\lambda^2}} \sum_{i=1}^{\infty} c_i e^{-Dk_i^2 t}\, {}_1F_1\Big(-\frac{\lambda^2 k_i^2}{2}; 1; \frac{r^2}{2\lambda^2}\Big). \tag{B.81}$$

B.12.2 Initial condition: uniform concentration

In the manuscript, we show three analytical solutions to the PDE with zero flux at the boundaries and each satisfying different initial conditions. We derive the three specific solutions in the following subsections. Here, we will tackle the uniform concentration initial conditions by examining the case where the concentration is 0 for $r \leq R_0$ and at uniform concentration c_0 for $r > R_0$. Once we have solved this general case, we will show the case where $R_0 = 0$.

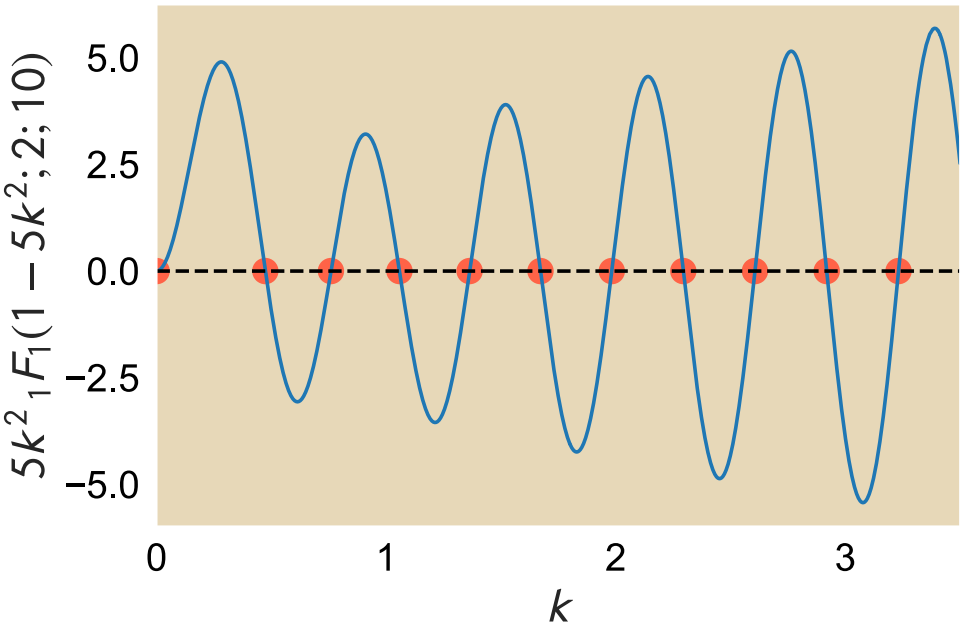

Figure B.10: **Zeros of k for $\frac{\lambda^2 k^2}{2}\,{}_1F_1\Big(1-\frac{\lambda^2 k^2}{2}; 2; \frac{R^2}{2\lambda^2}\Big) = 0$ where $\frac{R}{\lambda} = 3.16$.** Red dots are overlayed with the points where the Kummer confluent hypergeometric function crosses the x-axis.

The piecewise defined function then appears as

$$c(r,0) = \begin{cases} 0 & \text{if } r \le R_0, \\ c_0 & \text{if } r > R_0. \end{cases} \tag{B.82}$$

At $t = 0$, our equation looks like

$$c(r,0) = c_{\text{ss}}\, e^{-\frac{r^2}{2\lambda^2}} + e^{-\frac{r^2}{2\lambda^2}} \sum_{i=1}^{\infty} c_i \, {}_1F_1\Big(-\frac{\lambda^2 k_i^2}{2}; 1; \frac{r^2}{2\lambda^2}\Big), \tag{B.83}$$

We multiply both sides by the weighting function $w(r) = re^{\frac{r^2}{2\lambda^2}}$ and an eigenfunction of the differential equation $\Phi_h(r) = e^{-\frac{r^2}{2\lambda^2}} \, {}_1F_1\Big(-\frac{\lambda^2 k_h^2}{2}; 1; \frac{r^2}{2\lambda^2}\Big)$ for identifying the coefficients of the non-steady state terms or $\Phi_{\text{ss}}(r) = e^{-\frac{r^2}{2\lambda^2}}$ for determining the steady-state term. For the steady-state term, we have

$$\begin{aligned}
c_0 \int_{R_0}^{R} r \, \mathrm{d}r &= c_{\text{ss}} \int_0^R r\, e^{-\frac{r^2}{2\lambda^2}} \mathrm{d}r + \sum_{i=1}^{\infty} c_i \int_0^R r\, e^{-\frac{r^2}{2\lambda^2}} \, {}_1F_1\Big(-\frac{\lambda^2 k_i^2}{2}; 1; \frac{r^2}{2\lambda^2}\Big) \mathrm{d}r, \\
c_0 \frac{r^2}{2}\Big|_{R_0}^{R} &= -c_{\text{ss}} \lambda^2 e^{-\frac{r^2}{2\lambda^2}}\Big|_0^R + \sum_{i=1}^{\infty} c_i \int_0^R r \, {}_1F_1\Big(1 + \frac{\lambda^2 k_i^2}{2}; 1; -\frac{r^2}{2\lambda^2}\Big) \mathrm{d}r, \\
c_0\Big(\frac{R^2}{2\lambda^2} - \frac{R_0^2}{2\lambda^2}\Big) &= c_{\text{ss}}\Big(1 - e^{-\frac{R^2}{2\lambda^2}}\Big) + \sum_{i=1}^{\infty} \frac{c_i}{\lambda^2} \int_0^R \sum_{j=0}^{\infty} \mathrm{d}r\, r \, \frac{\Big(1 + \frac{\lambda^2 k_i^2}{2}\Big)_j}{(1)_j} \frac{\Big(-\frac{r^2}{2\lambda^2}\Big)^j}{j!}, \\
c_0\Big(\frac{R^2}{2\lambda^2} - \frac{R_0^2}{2\lambda^2}\Big) &= c_{\text{ss}}\Big(1 - e^{-\frac{R^2}{2\lambda^2}}\Big) - \sum_{i=1}^{\infty} c_i \sum_{j=0}^{\infty} \frac{\Big(1 + \frac{\lambda^2 k_i^2}{2}\Big)_j}{(1)_j} \frac{\Big(-\frac{r^2}{2\lambda^2}\Big)^{j+1}}{(j+1)!}\Big|_0^R.
\end{aligned} \tag{B.84}$$

We use the fact that $(1)_j = j!$ and $(j+1)! = (2)_j$ so

$$\begin{aligned}
c_0\Big(\frac{R^2}{2\lambda^2} - \frac{R_0^2}{2\lambda^2}\Big) &= c_{\text{ss}}\Big(1 - e^{-\frac{R^2}{2\lambda^2}}\Big) + \sum_{i=1}^{\infty} c_i \frac{r^2}{2\lambda^2} \sum_{j=0}^{\infty} \frac{\Big(1 + \frac{\lambda^2 k_i^2}{2}\Big)_j}{(2)_j} \frac{\Big(-\frac{r^2}{2\lambda^2}\Big)^j}{j!}\Big|_0^R, \\
c_0\Big(\frac{R^2}{2\lambda^2} - \frac{R_0^2}{2\lambda^2}\Big) &= c_{\text{ss}}\Big(1 - e^{-\frac{R^2}{2\lambda^2}}\Big) + \sum_{i=1}^{\infty} c_i \frac{r^2}{2\lambda^2} \, {}_1F_1\Big(1 + \frac{\lambda^2 k_i^2}{2}; 2; -\frac{r^2}{2\lambda^2}\Big)\Big|_0^R, \\
c_0\Big(\frac{R^2}{2\lambda^2} - \frac{R_0^2}{2\lambda^2}\Big) &= c_{\text{ss}}\Big(1 - e^{-\frac{R^2}{2\lambda^2}}\Big) + \sum_{i=1}^{\infty} c_i \frac{r^2}{2\lambda^2} e^{-\frac{r^2}{2\lambda^2}} \, {}_1F_1\Big(1 - \frac{\lambda^2 k_i^2}{2}; 2; \frac{r^2}{2\lambda^2}\Big)\Big|_0^R, \\
c_{\text{ss}} &= \frac{c_0}{2} \frac{\frac{R^2}{\lambda^2} - \frac{R_0^2}{\lambda^2}}{1 - e^{-\frac{R^2}{2\lambda^2}}},
\end{aligned} \tag{B.85}$$

where we use Eq. B.79 to remove the upper bound of the integral involving the hypergeometric function. We now find the coefficients for the non-steady state terms. We do so by multiplying both sides by $\Phi_h(r) = e^{-\frac{r^2}{2\lambda^2}}\,{}_1F_1\Big(-\frac{\lambda^2 k_h^2}{2}; 1; \frac{r^2}{2\lambda^2}\Big)$ instead,

$$\begin{aligned} c_0 \int_{R_0}^{R} r\,{}_1F_1\Big(-\frac{\lambda^2 k_h^2}{2}; 1; \frac{r^2}{2\lambda^2}\Big)\mathrm{d}r = c_{\mathrm{ss}} \int_0^R r e^{-\frac{r^2}{2\lambda^2}}\,{}_1F_1\Big(-\frac{\lambda^2 k_h^2}{2}; 1; \frac{r^2}{2\lambda^2}\Big)\mathrm{d}r \\ + \Bigg[\sum_{i=1}^{\infty} c_i \int_0^R r\, e^{-\frac{r^2}{2\lambda^2}}\,{}_1F_1\Big(-\frac{\lambda^2 k_i^2}{2}; 1; \frac{r^2}{2\lambda^2}\Big) \\ \times\,{}_1F_1\Big(-\frac{\lambda^2 k_h^2}{2}; 1; \frac{r^2}{2\lambda^2}\Big)\mathrm{d}r\Bigg]. \end{aligned} \tag{B.86}$$

Fortunately, we have already done the first integral on the right-hand side of the equation, so we only have to take care of the integral on the left-hand side. We further argue that by the Sturm-Liouville theory all of the integrals in the summation vanish except in the case where $i = h$. The equation then boils down to

$$\begin{aligned} c_0 \int_{R_0}^{R} r\,{}_1F_1\Big(-\frac{\lambda^2 k_h^2}{2}; 1; \frac{r^2}{2\lambda^2}\Big)\mathrm{d}r &= c_h \int_0^R r\, e^{-\frac{r^2}{2\lambda^2}} \Big[{}_1F_1\Big(-\frac{\lambda^2 k_h^2}{2}; 1; \frac{r^2}{2\lambda^2}\Big)\Big]^2 \mathrm{d}r, \\ c_0 \int_{R_0}^{R} \sum_{j=0}^{\infty} r \frac{\Big(-\frac{\lambda^2 k_h^2}{2}\Big)_j}{(1)_j} \frac{\Big(\frac{r^2}{2\lambda^2}\Big)^j}{j!}\mathrm{d}r &= c_h \int_0^R r\, e^{-\frac{r^2}{2\lambda^2}} \Big[{}_1F_1\Big(-\frac{\lambda^2 k_h^2}{2}; 1; \frac{r^2}{2\lambda^2}\Big)\Big]^2 \mathrm{d}r, \\ c_0 \sum_{j=0}^{\infty} \lambda^2 \frac{\Big(-\frac{\lambda^2 k_h^2}{2}\Big)_j}{(1)_j} \frac{\Big(\frac{r^2}{2\lambda^2}\Big)^{j+1}}{(j+1)!}\Bigg|_{R_0}^{R} &= c_h \int_0^R r\, e^{-\frac{r^2}{2\lambda^2}} \Big[{}_1F_1\Big(-\frac{\lambda^2 k_h^2}{2}; 1; \frac{r^2}{2\lambda^2}\Big)\Big]^2 \mathrm{d}r, \\ c_0 \frac{r^2}{2}\,{}_1F_1\Big(-\frac{\lambda^2 k_h^2}{2}; 2; \frac{r^2}{2\lambda^2}\Big)\Big|_{R_0}^{R} &= c_h \int_0^R r\, e^{-\frac{r^2}{2\lambda^2}} \Big[{}_1F_1\Big(-\frac{\lambda^2 k_h^2}{2}; 1; \frac{r^2}{2\lambda^2}\Big)\Big]^2 \mathrm{d}r, \\ c_h &= \frac{c_0}{2} \frac{R^2\,{}_1F_1\Big(-\frac{\lambda^2 k_h^2}{2}; 2; \frac{R^2}{2\lambda^2}\Big) - R_0^2\,{}_1F_1\Big(-\frac{\lambda^2 k_h^2}{2}; 2; \frac{R_0^2}{2\lambda^2}\Big)}{\int_0^R r\, e^{-\frac{r^2}{2\lambda^2}} \Big[{}_1F_1\Big(-\frac{\lambda^2 k_h^2}{2}; 1; \frac{r^2}{2\lambda^2}\Big)\Big]^2 \mathrm{d}r}, \end{aligned} \tag{B.87}$$

where we numerically integrate the denominator. When assembled together, the solution comes out to

$$c(r,t) = \frac{c_0}{2}\, e^{-\frac{r^2}{2\lambda^2}} \Bigg\{ \frac{\frac{R^2}{\lambda^2} - \frac{R_0^2}{\lambda^2}}{1 - e^{-\frac{R^2}{2\lambda^2}}} + \sum_{i=1}^{\infty} \frac{R^2\, {}_1F_1\Big(-\frac{\lambda^2 k_i^2}{2}; 2; \frac{R^2}{2\lambda^2}\Big) - R_0^2\, {}_1F_1\Big(-\frac{\lambda^2 k_i^2}{2}; 2; \frac{R_0^2}{2\lambda^2}\Big)}{\int_0^R r'\, e^{-\frac{r'^2}{2\lambda^2}} \Big[{}_1F_1\Big(-\frac{\lambda^2 k_i^2}{2}; 1; \frac{r'^2}{2\lambda^2}\Big)\Big]^2 \mathrm{d}r'} \times e^{-Dk_i^2 t}\, {}_1F_1\Big(-\frac{\lambda^2 k_i^2}{2}; 1; \frac{r^2}{2\lambda^2}\Big) \Bigg\}. \tag{B.88}$$

In the case where $R_0 = 0$, the solution for uniform concentration throughout the system is instead

$$c(r,t) = \frac{c_0}{2}\, e^{-\frac{r^2}{2\lambda^2}} \Bigg\{ \frac{\frac{R^2}{\lambda^2}}{1 - e^{-\frac{R^2}{2\lambda^2}}} + \sum_{i=1}^{\infty} \frac{R^2\, {}_1F_1\Big(-\frac{\lambda^2 k_i^2}{2}; 2; \frac{R^2}{2\lambda^2}\Big)}{\int_0^R r'\, e^{-\frac{r'^2}{2\lambda^2}} \Big[{}_1F_1\Big(-\frac{\lambda^2 k_i^2}{2}; 1; \frac{r'^2}{2\lambda^2}\Big)\Big]^2 \mathrm{d}r'} \times e^{-Dk_i^2 t}\, {}_1F_1\Big(-\frac{\lambda^2 k_i^2}{2}; 1; \frac{r^2}{2\lambda^2}\Big) \Bigg\}, \tag{B.89}$$

as shown in the manuscript.

B.12.3 Initial condition: Gaussian concentration for $r > R_0$

We finish the 2D advection-diffusion model with the initial condition of a Gaussian concentration profile outside of a region $r > R_0$ and 0 within that region. Written explicitly, the initial condition is

$$c(r,0) = \begin{cases} 0 & \text{if } r \le R_0, \\ c_0\, e^{-\frac{r^2}{2\lambda^2}} & \text{if } r > R_0. \end{cases} \tag{B.90}$$

We apply the same situation where we multiply both sides by the weighting function $w(r) = re^{\frac{r^2}{2\lambda^2}}$ and an eigenfunction of the differential equation $\Phi_h(r) = e^{-\frac{r^2}{2\lambda^2}}\, {}_1F_1\Big(-\frac{\lambda^2 k_h^2}{2}; 1; \frac{r^2}{2\lambda^2}\Big)$ for identifying the coefficients of the non-steady state terms or $\Phi_{\text{ss}}(r) = e^{-\frac{r^2}{2\lambda^2}}$ for determining the steady-state term. Relying on integrals performed in Subsec. B.12.2, we start with identifying the coefficients

of the dynamic terms c_i,

$$\begin{aligned}
\int_0^R c(r,0)w(r)\Phi_h(r)\mathrm{d}r &= c_{\mathrm{ss}}\int_0^R e^{-\frac{r^2}{2\lambda^2}}w(r)\Phi_h(r)\mathrm{d}r \\
&\quad+\sum_{i=1}^{\infty}c_i\int_0^R e^{-\frac{r^2}{2\lambda^2}}\,{}_1F_1\Big(-\frac{\lambda^2k_i^2}{2};1;\frac{r^2}{2\lambda^2}\Big) \\
&\quad\times w(r)\Phi_h(r)\mathrm{d}r, \\
c_0\int_{R_0}^R r\,e^{-\frac{r^2}{2\lambda^2}}\,{}_1F_1\Big(-\frac{\lambda^2k_h^2}{2};1:\frac{r^2}{2\lambda^2}\Big)\mathrm{d}r &= c_{\mathrm{ss}}\int_0^R r\,e^{-\frac{r^2}{2\lambda^2}}\,{}_1F_1\Big(-\frac{\lambda^2k_h^2}{2};1;\frac{r^2}{2\lambda^2}\Big)\mathrm{d}r \\
&\quad+\sum_{i=1}^{\infty}c_i\int_0^R w(r)\Phi_i(r)\Phi_h(r)\mathrm{d}r, \\
c_0\frac{r^2}{2}e^{-\frac{r^2}{2\lambda^2}}\,{}_1F_1\Big(1-\frac{\lambda^2k_h^2}{2};2;\frac{r^2}{2\lambda^2}\Big)\Big|_{R_0}^R &= c_h\int_0^R r\,e^{-\frac{r^2}{2\lambda^2}}\Big[{}_1F_1\Big(-\frac{\lambda^2k_h^2}{2};1;\frac{r^2}{2\lambda^2}\Big)\Big]^2\mathrm{d}r, \\
-c_0\frac{R_0^2}{2}e^{-\frac{R_0^2}{2\lambda^2}}\,{}_1F_1\Big(1-\frac{\lambda^2k_h^2}{2};2;\frac{R_0^2}{2\lambda^2}\Big) &= c_h\int_0^R r\,e^{-\frac{r^2}{2\lambda^2}}\Big[{}_1F_1\Big(-\frac{\lambda^2k_h^2}{2};1;\frac{r^2}{2\lambda^2}\Big)\Big]^2\mathrm{d}r, \\
c_h &= -c_0\frac{\frac{R_0^2}{2}e^{-\frac{R_0^2}{2\lambda^2}}\,{}_1F_1\Big(1-\frac{\lambda^2k_h^2}{2};2;\frac{R_0^2}{2\lambda^2}\Big)}{\int_0^R r\,e^{-\frac{r^2}{2\lambda^2}}\Big[{}_1F_1\Big(-\frac{\lambda^2k_h^2}{2};1;\frac{r^2}{2\lambda^2}\Big)\Big]^2\mathrm{d}r},
\end{aligned} \tag{B.91}$$

where we removed the terms $i \neq h$ as shown from Eq. B.66. To determine the initial conditions of the steady-state coefficient term, we would instead multiply by the weighting function and the steady-state eigenfunction $e^{-\frac{r^2}{2}}$ to yield

$$\begin{aligned}
c_0\int_{R_0}^R r\,e^{-\frac{r^2}{2\lambda^2}}\mathrm{d}r &= c_{\mathrm{ss}}\int_0^R r\,e^{-\frac{r^2}{2\lambda^2}}\mathrm{d}r+\sum_{i=1}^{\infty}c_i\int_0^R r\,e^{-\frac{r^2}{2\lambda^2}}\,{}_1F_1\Big(-\frac{\lambda^2k_i^2}{2};1;\frac{r^2}{2\lambda^2}\Big)\mathrm{d}r, \\
-c_0\,e^{-\frac{r^2}{2\lambda^2}}\Big|_{r=R_0}^R &= -c_{\mathrm{ss}}\,e^{-\frac{r^2}{2\lambda^2}}\Big|_{r=0}^R, \\
c_{\mathrm{ss}} &= c_0\frac{e^{-\frac{R_0^2}{2\lambda^2}}-e^{-\frac{R^2}{2\lambda^2}}}{1-e^{-\frac{R^2}{2\lambda^2}}}.
\end{aligned} \tag{B.92}$$

When all is assembled, the solution with the no-flux boundary conditions and FRAPed initial condition yields

$$c(r,t) = c_0\, e^{-\frac{v_{\mathrm{m}} r^2}{2DR}} \Bigg\{ \frac{e^{-\frac{v_{\mathrm{m}} R_0^2}{2DR}} - e^{-\frac{v_{\mathrm{m}} R}{2D}}}{1 - e^{-\frac{v_{\mathrm{m}} R}{2D}}} - \sum_{i=1}^{\infty} \frac{\frac{R_0^2}{2} e^{-Dk_i^2 t}\, {}_1F_1\Big(1 + \frac{DRk_i^2}{2v_{\mathrm{m}}}; 2; -\frac{v_{\mathrm{m}} R_0^2}{2DR}\Big)}{\int_0^R r\, e^{-\frac{v_{\mathrm{m}} r^2}{2DR}} \Big[{}_1F_1\Big(-\frac{DRk_i^2}{2v_{\mathrm{m}}}; 1; \frac{v_{\mathrm{m}} r^2}{2DR}\Big)\Big]^2 \mathrm{d}r} \, {}_1F_1\Big(-\frac{DRk_i^2}{2v_{\mathrm{m}}}; 1; \frac{v_{\mathrm{m}} r^2}{2DR}\Big) \Bigg\}. \tag{B.93}$$

B.13 Numerically solving advection-diffusion equations with COMSOL

COMSOL Multiphysics® simulations are constructed with consideration of four particular details in mind: design of the geometry, set-up of the differential equations, incorporation of images as initial conditions, and sweeping through parameters. A discussion of the mesh is discussed in Sec. B.14.

B.13.1 Geometry

Because simulations would be performed using images as initial conditions, and because the microtubule network has a roughly circular geometry, we designed a circle geometry in COMSOL where the radius was a parameter based upon the photobleach dataset used. This could range from as small as 70 µm for the networks nearing the end of contraction and upwards of 250 µm which sets the initial activation size for the experiments.

B.13.2 Setting up the differential equations

Although there are multiple partial differential equation forms in COMSOL that can be used for the advection-diffusion equation studied here, we elect to use the coefficient form PDE and define our variable of interest as u with units of mol/m^3 and a source term units of mol/(m^3·s). Although our past derivations use the variable c, we use u in the differential equation due to the occurrence of the coefficient c in the coefficient form PDE in COMSOL. We note that the coefficient form PDE as shown in COMSOL is of the form

$$e_a \frac{\partial^2 u}{\partial t^2} + d_a \frac{\partial u}{\partial t} + \nabla \cdot (-c\nabla u - \alpha u + \gamma) + \beta \cdot \nabla u + au = f, \tag{B.94}$$

where e_a, d_a, c, a, and f are scalar coefficients while α, γ, and β are vectors. We note that since our advection-diffusion (using u for concentration here) is of the form

$$\frac{\partial u}{\partial t} = D\nabla^2 u + \frac{v_{\mathrm{m}}}{R} \nabla \cdot (\mathbf{r} u)\,, \tag{B.95}$$

if we rewrite the equation a little bit to match the form of Eq. B.94, we get

$$\frac{\partial u}{\partial t} + \nabla \cdot \left(-D\nabla u - \frac{v_{\mathrm{m}}}{R}\mathbf{r}u \right) = 0. \tag{B.96}$$

We can see here that to make Eq. B.96 match Eq. B.94, then e_a, a, all of the elements of γ, all of the elements of β, and f are all 0 while

$$d_a = 1 \text{ s}^{-1}, \tag{B.97}$$

$$c = D, \tag{B.98}$$

$$\alpha = \begin{bmatrix} \frac{v_{\mathrm{m}}}{R}x \\ \frac{v_{\mathrm{m}}}{R}y \end{bmatrix}, \tag{B.99}$$

where we note that we define D to take on dimensions of length^2/time and $\frac{v_{\mathrm{m}}}{R}$ to have units of time^{-1} in COMSOL.

In our experiments, we were careful to ensure that there was negligible to no detectable amount of microtubules flowing from outside of the light-activated region into network. We similarly impose a no-flux boundary condition by using the Zero Flux boundary condition option in COMSOL.

B.13.3 Incorporation of images as initial conditions

One of the conveniences of using COMSOL is the ability to use experimental data as part of the simulations. Here, we elected to use the first photobleached frame as our initial condition for our images. Before doing so, we took our image of interest and imposed a small Gaussian smoothing ($\sigma = 1$pixel) to gently smooth out the microtubule concentration field before renormalizing the image and returning it into an 8-bit image ('uint8'). We then exported the image as a TIFF file. Within COMSOL, under our Component $\rightarrow$ Definitions branch of the simulation, we defined an Image Function and gave it the notation u_im. Within the image function, we selected the image of interest under the Browse option. We then need to line up the image such that the center of the contracting microtubule network is at the origin or else the advection-diffusion model will drive the advective contraction toward a different part of the network. To do so, we specify the coordinates where we determine the minimum and maximum x and y values based on the pixel-weighted center of the network as discussed in Appendix B.2 and dimensions of the image. We then import the image and verify the image was the one we wanted by plotting.

When incorporating the image in COMSOL, under the Coefficient Form PDE node in the Initial Conditions tab, we set the initial time derivative of u to 0 while the initial value for u is set as $u\_im(x, y)$, where (x, y) specifies the spatial dimensions of the image. Fortunately, by the geometry we specify, we will not pick up any parts of the image outside of the region of interest. We further multiply this function by a coefficient such that we obtain roughly the correct units of concentration as required.

B.13.4 Parameter sweep

To perform the parameter sweep, we include the Parametric Sweep option in the Study section of the simulation and define the parameters of interest under Global Definitions → Parameters. Within the parameters, we specify the parameters D for our diffusion constant and *alpha* for our contraction rate, which replaces $\frac{v_m}{R}$ in the equations above, including our definition of α in Eq. B.99. Under the Parametric Sweep, we can then chose D and *alpha* as our parameters to be swept. By selected our range of *alpha* to be 0.0016 to 0.0024 s^{-1} in increments of 0.0002 s^{-1} while D ranged from 0.05 to 0.2 $\mu m^2/s$ in increments of 0.05 $\mu m^2/s$. All possible combinations of D and *alpha* were permitted for the simulations.

B.14 Gibbs phenomenon in analytical solutions and mesh granularity in FEM

A common observation found for many of the analytical solutions is the disagreement between the analytical solution at $t = 0$ and the defined initial condition that the solution is intended to recapitulate. As shown in Fig. 1 of the main manuscript, the analytical solution, which is composed of twelve nonzero eigenvalues and the steady-state function, creates oscillations about the intended initial condition. This disagreement is a demonstration of the Gibbs phenomenon, as famously revealed by the imperfect decomposition of a square wave into a sum of sinusoidal functions. Fig. B.12 demonstrates the evolution of each of the three analytical solutions examined in the main manuscript when more eigenvalues are included in the solution. Specifically, for $c(r, 0) = c_0$ (Fig. B.12A), $c(r > R_0, 0) = c_0$ (Fig. B.12B), and $c(r > R_0, 0) = c_0 \exp(-r^2/2\lambda^2)$ (Fig. B.12C), all of which are represented by dashed black lines, more eigenvalues reduce the level of error between the analytical solution and the initial condition. For the two initial conditions involving a uniform concentration, the

use of one eigenvalue in addition to the steady-state solution (purple line) leads to a large negative concentration at $r = 0$ but begins to better recapitulate the initial conditions by the addition of 12 non-zero eigenvalues. Deviations from the initial condition decrease dramatically by that point. This is further observed for the clipped Gaussian distribution: while the Gaussian tail is quantitatively captured by the the addition of only a few eigenvalues, the analytical solution begins to better recapitulate the concentration profile about $r = R_0$ with the addition of more terms in the solution. Nevertheless, even after using twelve eigenvalues, the solution shows small oscillations about the exact initial condition and is a continued feature with the addition of more eigenvalues.

The deviations in the constructed solutions from the true values are also apparent in finite element methods through the choice of granularity in the mesh. As FEM involves solving the governing equation over a particular domain, having a very fine grained mesh allows for the FEM solution to more accurately reflect the true solution to the problem at the cost of computational time. On the other hand, a very coarse-grained mesh involves less computing power to solve the original equations but may coarse grain away details smaller than the element size, requiring a balance between accurately solving the original PDE(s) and computational efficiency.

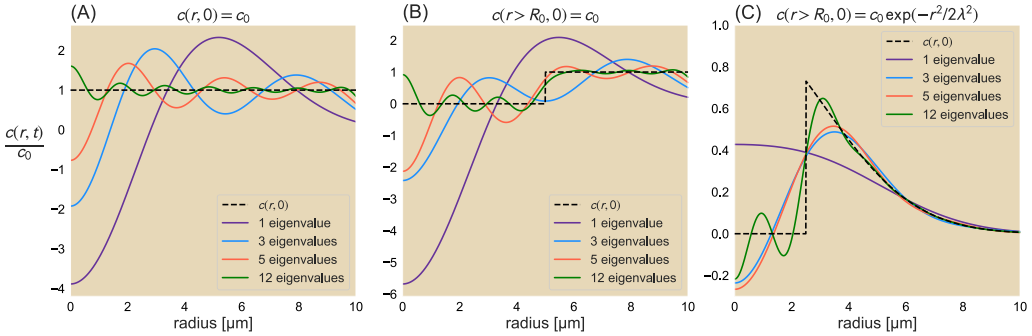

Figure B.11: **Gibbs phenomenon for analytical solutions.** Concentration profiles of the analytical solution for the initial conditions (A) $c(r, 0) = c_0$, (B) $c(r > R_0, 0) = c_0$, and (C) $c(r > R_0, 0) = c_0 \exp(-r^2/2\lambda^2)$ with the steady-state solution and the first nonzero eigenvalue solution (purple line), the first three nonzero eigenvalue solutions (blue), the first five terms (red), and the first twelve terms (green). The intended initial conditions are represented as dashed black lines.

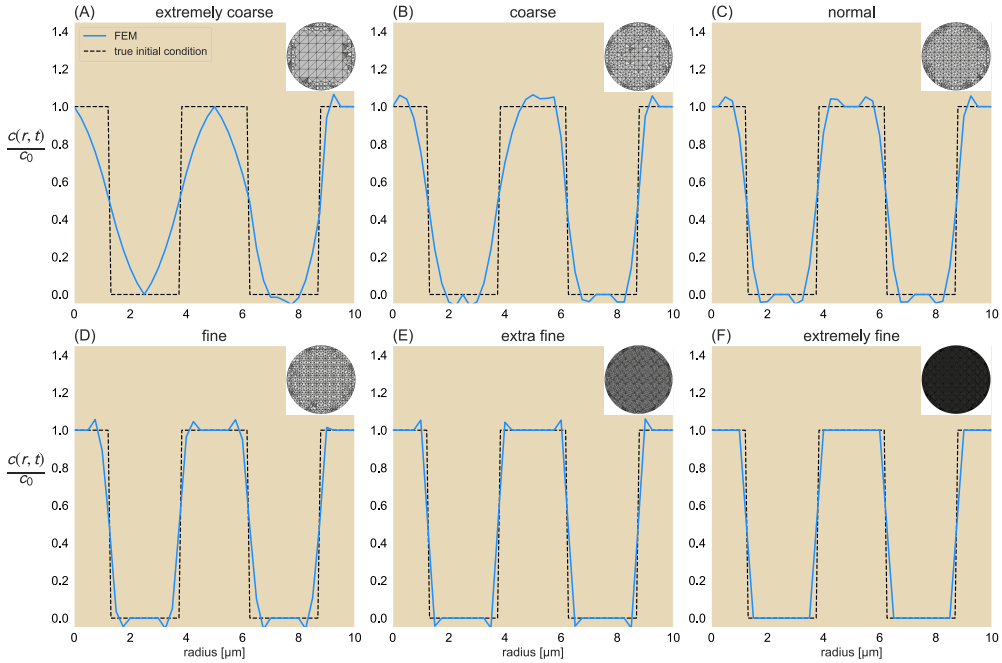

Figure B.12: **Effects of mesh granularity on FEM solution.** Concentration profiles at $t = 0$ for six different element sizes as defined by the COMSOL Multiphysics physics-controlled mesh: (A) extremely coarse, (B) coarse, (C) normal, (D) fine, (E) extra fine, and (F) extremely fine. Finite elements output is represented by the blues lines while the true initial conditions are given as the black dashed lines. For visualization purposes, the appearance of the meshes used for the defined geometry are shown as insets in the upper right-hand corner of the respective subfigures. Concentration profile is from a line trace along the horizontal axis from the origin of the geometry to the boundary.

Fig. B.12 shows how the granularity of the mesh affects the FEM solutions. We compare the concentration profiles produced by FEM (solid blue lines) against the true initial condition (dashed black lines) for six different element sizes as found in the physics-controlled mesh feature in COMSOL Multiphysics: (A) extremely coarse, (B) coarse, (C) normal, (D) fine, (E) extra fine, and (F) extremely fine. We see that using the most coarse-grained feature produces a more sinusoidal shape of matching frequency and amplitude to the square wave pattern of the initial condition. However, with successive decreases in element size (increase in mesh fineness) the FEM solution more closely reflect the initial condition. Fig. B.12B-E show that increase the mesh fineness leaves fewer deviations from the true values, largely located near the discontinuities in the profile. The insets in the upper right of each figure shows the mesh pattern for the geometry for the study. As Fig. B.12F shows, while the extremely fine

mesh does not overshoot above the c_0 values or undershoot the $c(r,0) = 0$ regions, the finite size of the elements in the mesh causes the discontinuous region to take on a value between the two regions instead.

B.15 Parameter sweeping and Péclet numbers

In this section, we ask how changes in the diffusion constant D and contraction velocity v_m are reflected in the grid patterned advection-diffusion model. This interplay reveals itself by transforming Eq. B.19 into dimensionless form. Suppose instead of v_max we wrote that out as a function of the speed of individual motors which move along and move microtubules. We noted that the maximum velocity occurred at the outer edge of the activation circle. Assuming a telescoping model where a filament network contracts due to a series of alternating filaments and motors connecting them, we start by treating the maximum velocity as the speed of the motors multiplied by the minimum number of filaments required to connect the origin to the outer edge of the activation zone. This is simply a case of filaments being serially aligned at their ends. This scheme then means that for a filament of average length L and activation circle of radius R

$$v_\mathrm{m} = v_L \frac{R}{L} \tag{B.100}$$

where v_L is a natural velocity scale. If we further redefine some variables to make them dimensionless, such as $x \to L\tilde{x}$ and $t \to \frac{L}{v_L}\tilde{t}$, we can alter Eq. B.68 to

$$\begin{aligned}
\frac{\partial c}{\partial t} &= D\nabla^2 c - \nabla\cdot(\mathbf{v}c)\,, \\
&= D\nabla^2 c + \frac{v_\mathrm{m}}{R}\nabla\cdot(\mathbf{r}c)\,, \\
\frac{v_L}{L}\frac{\partial c}{\partial \tilde{t}} &= \frac{D}{L^2}\tilde{\nabla}^2 c + \frac{v_L}{L}\tilde{\nabla}\cdot(\tilde{\mathbf{r}}c), \\
\frac{\partial c}{\partial \tilde{t}} &= \frac{D}{v_L L}\tilde{\nabla}^2 c + \tilde{\nabla}\cdot(\tilde{\mathbf{r}}c)\,, \\
\frac{\partial c}{\partial \tilde{t}} &= \frac{1}{\mathrm{Pe}}\tilde{\nabla}^2 c + \tilde{\nabla}\cdot(\tilde{\mathbf{r}}c)\,,
\end{aligned} \tag{B.101}$$

where Pe is the Péclet number:

$$\mathrm{Pe} \equiv \frac{v_L L}{D}. \tag{B.102}$$

This dimensionless parameter tells us how the contraction speed of a connected network and the diffusion constant dictate whether the contraction process

or diffusion process dominates. For fixed length L such as the length of a microtubule, increasing Péclet number tells us that the advection is dominant and thus Eq. B.101 is largely the advective term, while smaller values of Pe tell us that diffusion is the dominant term.

Amusingly, had we defined the natural time variable to be $\tilde{t} = \frac{D}{L^2}t$, then Eq. B.101 would be modified as

$$\frac{\partial c}{\partial \tilde{t}} = \tilde{\nabla}^2 c + \mathrm{Pe}\tilde{\nabla} \cdot (\tilde{\mathbf{r}}c), \tag{B.103}$$

Pe illustrates the relationship between the advection in the system and the diffusion. For the parameters used for Fig. 4, if we take the characteristic length scale to be on the order 1, roughly the length of the microtubule in our experiments (see Appendix B.6 then $v_{\mathrm{L}} = 0.01\ \frac{\mu\mathrm{m}}{\mathrm{s}}$ and we obtain a Péclet number of 0.1. As this value is much smaller than unity, we see that the diffusion term dominates over the short timescale.

To further demonstrate the tradeoffs between advection and diffusion, we examined the redistribution of the concentration with the same gridlike pattern for different Péclet numbers. To do so, we kept v_{m} fixed and varied D for a set of simulations while for another set of FEM studies we kept D fixed while changing v_{m}. Fig. B.13 shows the concentration along the x-axis that extends from the origin to the boundary at $r = 10$ µm and as depicted by the purple line in the $t = 0$ plot in Fig. 4A. Fig. B.13A looks at a time series of the concentration profile for different diffusion constants while v_{m} is fixed at 0.1 $\frac{\mu\mathrm{m}}{\mathrm{s}}$ while Fig. B.13B shows the concentration profile for different v_{m} with D kept constant at 0.1 $\frac{\mu\mathrm{m}^2}{\mathrm{s}}$. Using the purple line in Fig. B.13A as the original parameter combination used in Fig. 4, we see that increasing the diffusion constant (green and blue) causes the individual squares of initial concentration c_0 to quickly disperse to create a more uniform concentration before the advection creates the Gaussian steady-state profile (and ones with longer standard deviations than the original parameters). This observation makes sense as the Péclet number gets lower and lower with increases in D, causing the diffusion term to dominate more than the advection. This increase in diffusion further illustrates the wider Gaussian distribution obtained at steady state, as the length scale λ depends on the square root of D and inversely on the advection speed v_{m}.

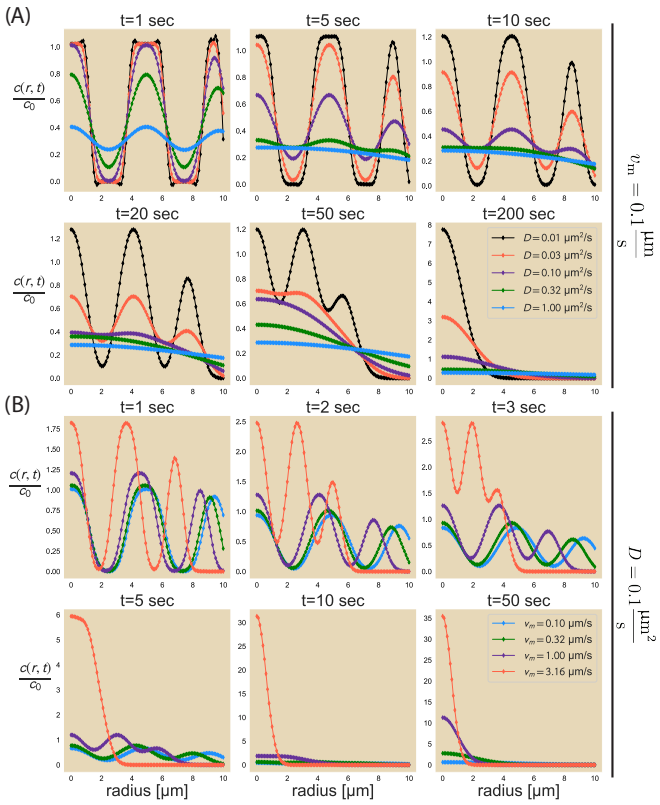

Figure B.13: **Traces of concentration as a function of radius for various combinations of diffusion constant D and velocity $v_{\mathbf{m}}$.** (A) Concentration profiles for D spanning three orders of magnitude with the velocity fixed at $v_{\mathrm{m}} = 0.1\,\frac{\mu\mathrm{m}}{\mathrm{s}}$. As shown in the yellow boxes for the heatmap for $t = 0$ sec, the concentration throughout the black gridlines is 0 while the concentration in the white cells is constant c_0. (B) Concentration profiles for varying v_{m} with the diffusion constant fixed at $D = 0.1\,\frac{\mu\mathrm{m}^2}{\mathrm{s}}$ Traces of all concentration profiles are obtained from a 1D slice along the x-axis from the origin of the circle to the boundary at $R = 10$ μm as shown by the purple line in Fig. 4A.

In contrast, decreasing the diffusion constant which increases the Péclet number preserves the oscillatory pattern of the concentration profile as the advection pushes the material toward the origin. We see that by $t = 50$ sec, the red and black curves that denote $D = 0.03\,\frac{\mu\mathrm{m}^2}{\mathrm{s}}$ (Pe $= 0.3$) and $D = 0.01\,\frac{\mu\mathrm{m}^2}{\mathrm{s}}$ (Pe $= 1.0$), respectively, still exhibit wave-like shapes at the $t = 50$ sec mark. As a result of the reduced diffusive effects, the concentration at the center is much higher and falls off much more quickly as the length scale λ is shorter (1.7 μm for the red curve and 1 μm for the black curve).

Tuning the advection for fixed diffusion constant as shown in Fig. B.13B similarly demonstrates the competition between diffusion attempting to level out

the concentration profile and advective flow trying to concentrate molecules toward the center. With the purple line corresponding with Pe = 1, we see that decreasing advection and lowering Pe, as demonstrated earlier, causes the differences between local minima and maxima in concentration to decrease faster than the minima and maxima move toward the origin. On the other hand, by increasing v_{m} and thus increasing Pe to make advection more dominant (red line of Fig. B.13B), we see that the advective flow causes the minima and maxima to be pushed toward the origin in less than 5 sec and create a sharper Gaussian peak (a discussion about the jagged profile for the $v_{\mathrm{m}} = 3.16\,\frac{\mu\mathrm{m}}{\mathrm{s}}$ plot can be founded in the Appendix on the Gibbs phenomenon and FEM mesh setting). Taken together, when diffusion dominates Pe < 1 the concentration of molecules tends toward a more uniform behavior before advection pushes them to the origin, causing peaks and troughs in the concentration to disperse and become indistinguishable. On the other hand, when advection dominates Pe > 1 peaks and troughs move toward the origin faster than they disperse, and lead to more tightly distributed Gaussian steady-state profiles.

BIBLIOGRAPHY

[1] T. D. Ross et al., "Controlling organization and forces in active matter through optically defined boundaries", Nature 572 (2019), 224.

[2] N. Georgoulia, *Tubulin polymerization with GTP/GMPCPP/Taxol*, 2012.

[3] S. J. DeCamp, "*Dogic lab - acrylamide coating protocol.*", (2016).

[4] G. W. Zack, W. E. Rogers, and S. A. Latt, "Automatic measurement of sister chromatid exchange frequency", Journal of Histochemistry and Cytochemistry 25 (1977).

[5] B. Carpenter et al., "Stan: A probabilistic programming language", J Stat Softw 76 (2017).

[6] W. Niblack, *An Introduction to Digital Image Processing*, Prentice-Hall, 1986.

[7] R. A. Banks, V. Galstyan, H. J. Lee, S. Hirokawa, A. Ierokomos, T. Ross, Z. Bryant, M. Thomson, and R. Phillips, "Motor processivity and speed determine structure and dynamics of motor-microtubule assemblies", bioRxiv (under review at eLife) (2021).

[8] N. F. Endres et al., "A lever-arm rotation drives motility of the minus-end-directed kinesin Ncd", Nature 439 (2006), 875.

[9] G. Guntas et al., "Engineering an improved light-induced dimer (iLID) for controlling the localization and activity of signaling proteins", Proc Natl Acad Sci 112 (2015), 112.